Pure Appl. Geophys. 178 (2021), 5031–5059

https://doi.org/10.1007/s00024-020-02614-w

Pure and Applied Geophysics

A Numerical Model for Tsunami-Induced Morphology Change

Babak Tehranirad,[1,2] James T. Kirby,[1] and Fengyan Shi[1]

Abstract—We describe the development of a time-resolved model for tsunami-induced morphology change, based on an existing Boussinesq model for weakly-dispersive free-surface waves coupled to a depth-integrated model for sediment concentration and an equation for bed level change. The model allows for spatial variability in bottom friction coefficients and accounts for the presence of non-erodible beds or finite depths of available sediment. The model is verified using one laboratory data set and against field observations of morphology change in the Crescent City, CA harbor during the 2011 Tohoku tsunami event. The model is then applied to a hypothetical example illustrating the impact of tsunami inundation on an undeveloped barrier island.

Keywords: Tsunami, sediment transport modeling, morphology change.

1. Introduction

Tsunamis can cause significant changes to coastal morphology. Recent events have provided numerous examples of erosion of barrier islands, sand dunes and coastal protection systems (Choowong et al. 2008; Fritz 2011; Gelfenbaum and Jaffe 2003; Goto et al. 2011, 2012a, b; Gusman et al. 2018; Haraguchi et al. 2012; Naruse and Abe 2017; Ramalho et al. 2018; Sugawara et al. 2014a, b; Szczuciński et al. 2012; Takashimizu et al. 2012; Tanaka et al. 2012; Tanaka and Sato 2015; Udo et al. 2012, 2016; Wilson et al. 2012). Post-tsunami measurements suggest that during tsunami inundation significant amounts of sand are eroded from sandy coasts and deposited further onshore (Goto et al. 2011, 2012a; Udo et al. 2016). In many cases, dune protection systems were completely eroded, where eroded sediment deposited onshore behind the dunes (Haraguchi et al. 2012). After the 2004 Indian Ocean Tsunami on the western coast of Thailand, field surveys showed that coastal dunes close to the shoreline were the source for sand deposits extending 1 km onshore, covering the low-lying coastal areas (Choowong et al. 2008; Hori et al. 2007). The 2011 Tohoku-oki tsunami, which devastated the most tsunami-prepared coastline in the world, further revealed the potential for tsunamis to change coastal morphology in sandy regions (Goto et al. 2012a, b; Takashimizu et al. 2012; Udo et al. 2012, 2016). Significant morphological changes were observed on coasts with intermittent coastal protection, where severe damage and erosion in less protected areas were observed (Goto et al. 2012a; Tanaka et al. 2012).

In addition to sandy coasts, tsunami-induced morphological impacts has been significant in other coastal areas, especially in regions neighboring coastal structures. Considerable erosion and deposition has been observed inside harbors during recent events. During the 1960 Chilean tsunami, sediment up to 4 m thick was deposited in parts of Crescent City harbor in California, while major scouring around coastal structures was observed (Lander et al. 1993). A similar amount of deposition was reported by Goto et al. (2011) for Kirinda Harbor in Sri Lanka after the 2004 Indian Ocean tsunami. After the 2011 Tohoku-Oki tsunami, although there was no record of any significant inundation on the west coast of the US, Wilson et al. (2012) reported that the tsunami generated strong currents inside Crescent City and Santa Cruz harbors, and caused considerable morphological change. Inside Crescent City harbor, scour of 289,400 m^3 was observed in an area of 0.67 km^2. Such sediment action can significantly affect the stability of coastal structures (Goto et al. 2012a; Yeh

[1] Department of Civil and Environmental Engineering, Center for Applied Coastal Research, University of Delaware, Newark, DE 19716, USA. E-mail: btrad@udel.edu

[2] *Present Address*: USGS Pacific Coastal and Marine Science Center, 2885 Mission St, Santa Cruz, CA 95060, USA.

et al. 2005), especially during tsunami rundown, when water levels decrease and result in a drop in the effective stress around the structure (Goto et al. 2012b).

Field observations suggest that tsunami sediment transport is mainly limited to shallow water and onshore, and is most significant during rundown. Goto et al. (2012a, b) and Udo et al. (2016) have concluded that, for the Tohoku-Oki tsunami, most of the sediment deposited inland originated from dune erosion. Although Gelfenbaum and Jaffe (2003) suggest that sediments originating in water depths of 20–800 m were the main sources for inland tsunami deposition during the 1998 Papua New Guinea event, for most scenarios, onshore sandy deposits originated primarily from beach and sand dune erosion (e.g. Szczuciński et al. 2012). Many researchers have also pointed out that large sediment action occurs during tsunami rundown (Choowong et al. 2008; Goto et al. 2012a, b; Tanaka et al. 2012; Udo et al. 2012).

Although tsunamis-induced morphological changes are expected to be significant in the vicinity of coastal structures and on sandy coasts, there is a shortage of appropriate models that can properly capture this process. Consequently, efforts to model tsunami-induced sediment transport are becoming more frequent, with models increasingly verified in comparison to both laboratory and field observations (Apotsos et al. 2011; Kim 2015; Klonaris et al. 2017; Li and Huang 2013; Rasyif et al. 2019; Sanchez et al. 2016; Son and Jung 2015; Yamashita et al. 2016). Li and Huang (2013) have studied the change of beach profile under tsunami waves using XBEACH and Delft3D. They simulated sediment movement during tsunami conditions for both laboratory and field test cases with different sediment pickup functions and reported that Van Rijn (1986) formulation performed better for tsunami conditions compared to other available formulas. More recently, modelers have incorporated sediment transport models within Boussinesq-type hydrodynamic models (Kim et al. 2017; Klonaris et al. 2017; Long et al. 2006; Rahman et al. 2012; Teran Cobo et al. 2006). Many of these models focused on modeling short-wave sediment transport modeling or were not set up to consider the effects of coastal structures and non-erodible regions on tsunami-induced morphological changes, which is an essential part of modeling morphological impacts in urban areas.

In this study, we couple the Boussinesq model FUNWAVE-TVD (Shi et al. 2012) with a depth-integrated Advection-Diffusion (AD) sediment transport module, and a morphology scheme which includes treatment of non-erodible beds as well as slope-limitation using an avalanching scheme. In Sect. 2, we describe the governing equations and model implementation. In Sect. 3, we verify the model using a simulation of tsunami-induced morphological change in Crescent City, CA harbor during the 2011 Japan tsunami. In Sect. 4, we investigate the hypothetical effect of tsunami morphological adjustment on an undeveloped sandy barrier island located on the US East Coast. Discussion of future development and needs as well as conclusions are provided in Sect. 5.

2. *Combined Wave-Sediment Transport-Morphology Model*

Significant progress has been made in the accurate simulation of tsunami hydrodynamics, using increased computational power and development of higher-order numerical schemes (Kim et al. 2009; Shi et al. 2012). The model developed here uses the wave-resolving Boussinesq model FUNWAVE-TVD (Shi et al. 2012) in conjunction with a depth-integrated model for total sediment load and an equation for the change in bed elevation. FUNWAVE-TVD has been extensively described elsewhere; readers may refer to the original work of Shi et al. (2012) for details of the model formulation and numerical implementation using a hybrid finite volume/finite difference approach. Here, we concentrate on the added components of the model system related to sediment transport and bed level change.

2.1. *Governing Equations for Sediment Motion*

We employ a depth-averaged Advection-Diffusion (AD) equation for suspended sediment concentration, given by

$$(\overline{c}H)_{,t} + \nabla_h \cdot \mathbf{q}_s = \nabla_h \cdot (kH\nabla_h \overline{c}) + P - D \qquad (1)$$

where $\overline{c}$ is depth-averaged sediment concentration and $H = h + \eta$ is local total water depth, both in a wave-resolved sense. $\mathbf{q}_s = \overline{c}H\overline{\mathbf{u}}$ is the horizontal advective flux of suspended sediment, k is a horizontal diffusion coefficient, $\overline{\mathbf{u}}$ is the depth-averaged velocity, P and D are pickup and deposition rates, and ∇_h is the horizontal derivative function. Details of the derivation of the depth-integrated AD model and modeling choices for all parameters are described in "Appendix A".

2.2. Bed Evolution Model

Changes in the local bed elevation $-h(\mathbf{x}, t)$, with bed load neglected, depend entirely on the imbalance in the local pickup and deposition rates P and D, or

$$h_{,t} = \frac{1}{1-n}\left(\overline{P} - \overline{D}\right) \tag{2}$$

with an excess of pickup over deposition causing an increase in depth. Here, quantities with overlines indicate values which have been averaged over some range of hydrodynamic time steps in order to represent values depending on a larger morphology time step, as described in "Appendix A.5". n is the sediment porosity. Corrections to this approach are required near the shoreline, where conservation problems may arise due to the intermittency of inundation. This issue is addressed further in "Appendix A".

In this study, we neglect bed load, which is the transport of particles by rolling along the bed surface, because morphological changes under the tsunami condition is dominated by suspended sediment transport (Goto et al. 2011). Tehranirad et al. (2016) investigated whether the bed load is negligible for tsunami flow conditions using Van Rijn (2007a, b)'s definition of suspended and bed loads, and showed that, for coarse sand ($d_{50} \simeq 1mm$), the bed load is less than 5% of the suspended load, with the ratio even smaller for fine sand ($d_{50} < 0.2mm$). Accordingly, we neglect bed load effects in the present analysis.

2.3. Non-erodible Beds

Non-erodible surfaces are expected to occur frequently during overland flooding processes. Here, we define a rigid, non-erodible surface to be located at elevation $z = -h_s(\mathbf{x})$. This surface may be exposed (or $h_s = h$) or it may lie below the actual bottom, giving an erodible sediment layer of thickness $t_s = h_s - h$ (Fig. 1). Because the bed load is neglected in our computation, the hard bottom methodology can be easily implemented by forcing the pickup rate P to be zero wherever there is no erodible sand. Therefore, the hard bottom condition can be described as,

$$P = \bar{P} = 0; \qquad h(\mathbf{x}, t) = h_s(\mathbf{x}) \tag{3}$$

This condition is implemented both in the AD and sediment continuity equations.

2.4. Slope Limiting Methodology

We use an avalanching algorithm to control the maximum bottom slope. By definition, the bottom slope cannot exceed the angle of repose ϕ of the sediment; avalanching occurs to reform a bed with the maximum slope angle equal to ϕ, usually between 25° and 40°. ϕ is dependent on bed material properties, and can be specified in the model input. We use the method of Larson and Kraus (1989) to limit the bed slope. The implementation of the avalanche scheme is further described in Tehranirad et al. (2016).

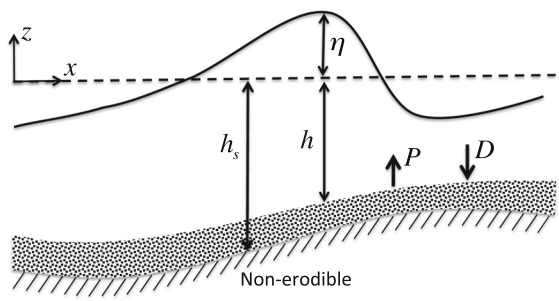

Figure 1
Nomenclature used in model description. P and D represent local pick-up and deposition rates

2.5. Conservation of Sediment

It is essential for any sediment transport simulation to conserve sediment throughout the modeling process. The model must assure that the amount of sand eroded from the bed is equal to the amount of suspended sediment in the water columns. Using (2) in (1) and integrating over a time-independent area A, we obtain

$$\left[\int_A (\overline{c}H - (1-n)h)dA\right]_{,t} = -\oint_{\delta A} \mathbf{n}\cdot(\mathbf{q}_s - kH\nabla_h\overline{c})ds\cdot\mathbf{n}ds \quad (4)$$

where δA is the boundary of the area A, $\mathbf{n}$ is the outward-pointing unit normal on the boundary, and n is the sediment porosity. The first term is more easily interpreted using an expression for depth h that is divided between a reference depth $h_0(\mathbf{x})$ and a deviation $\delta h(\mathbf{x},t)$ that represents temporal changes due to erosion or deposition. h in (4) may then be replaced by δh, and the first integral represents the total volume of sediment stored in suspension and eroded from the bed. The second integral represents the total flux of sediment across the region boundary due to advection and diffusion. After the avalanching procedure is implemented, and the sand conservation checked, the updated bed information is transferred to the Boussinesq model.

Numerical implementation of the model is discussed briefly in "Appendix A", with full details given in Tehranirad et al. (2016). Tehranirad et al. (2016) provide documentation of a pure advection test which compares the present scheme and a lower-order upwind scheme employed in Buttolph et al. (2006) and illustrates the relatively non-diffusive behavior of the scheme used here.

3. Model Verification

In this section, we present the results of a model validation conducted using simulations of a field case. The field case considers morphology changes in the Crescent City, CA harbor during the 2011 Tohoku-oki tsunami. The availability of the data along with a tested source model for the event (Grilli et al. 2013; Kirby et al. 2013), as well as an environment where the hard bottom condition of the model could be tested in complex bathymetries, were the reasons this test was chosen here. Additional tests for the solitary wave experiments of Kobayashi and Lawrence (2004), and dam-break test of Pintado-Patiño (2017) may be found in Tehranirad et al. (2016, 2017).

3.1. Effects of the Tohoku-oki 2011 Tsunami in Crescent City, CA Harbor

Two recent tsunami events affected the west coast of the United States, one originating off the coast of Chile on February 27, 2010, and the other off Japan on March 11, 2011. Both tsunami events created strong currents within harbors in California, causing up to $50 million in damage (Wilson et al. 2012, 2013). During the 2011 tsunami, the maximum tsunami amplitude was measured at 2.47 m in Crescent City harbor. In California, the most severe tsunami effects were observed in Crescent City harbor, a harbor known for vulnerability to tsunamis because of offshore bathymetry and the harbor configuration (Horrillo et al. 2008; Kowalik et al. 2008). During the first two hours of tsunami activity, the tide gauge recorded a peak amplitude of almost 2.5 m, which fortunately occurred at low tide, producing very limited inundation of dry land. Video analysis indicated peak currents of 4.5 m/s at the mouth of the basin (Wilson et al. 2012). Some overland flooding was observed in the recreational vehicle parking near the mouth of Elk River, while all docks inside the small boat basin were extensively damaged or destroyed during the tsunami.

Because of tide-gauge recordings as well as the availability of pre- and post-tsunami bathymetry measurements, we decided to simulate 2011 Tohoku-oki morphological effects inside Crescent City harbor. This test case examines whether the model can work effectively in complex bathymetric conditions, where the hard bottom condition of the model could be tested in areas with breakwater, jetties, and seawalls.

3.1.1 Pre- and Post-event Field Measurements

Wilson et al. (2012) investigated two sets of pre- and post-tsunami bathymetric data for the Crescent City harbor to assess the morphological changes induced by 2011 tsunami. They concluded that the best comparison could be obtained from NOAA's multi-beam bathymetry collected on November 18–23 2008 and March 17–21, 2011 (NOAA, 2008 and NOAA, 2011). The difference between these datasets is shown in Fig. 2. Figure 2 shows the overlap area between two datasets where about 289,360 m^3 of sediment was scoured and an approximate 154,600 m^3 of sediment deposition was observed. However, the surveys do not extend throughout all parts of the harbor, and they do not include deposition in the west of the small boat basin. Wilson et al. (2012) reported that significant deposition within portions of the mid-harbor and the small boat basin rendered much of the inner harbor unusable for navigation.

Through the analysis of videos, as well as pre- and post-tsunami bathymetric datasets, Wilson et al. (2012) were able to provide a detailed picture of how sediment transport occurred during the 2011 tsunami in Crescent City harbor. They reported that during the most active parts of the 2011 tsunami, water rapidly surged into and out of the outer harbor entrance, causing bathymetric changes inside the harbor. Admire et al. (2014) later confirmed that the currents within the harbor peaked at a velocity of 4.5 m/s, and created at least six cycles with velocities exceeding 3 m/s. Significant scouring was observed close to the jetties, with as much as 4 m of scouring occurring off the jetty tip. The erosional pattern continued along the backside of the jetty and into the south-east portion of the mid-harbor. The tsunami also scoured the mid-harbor area and the region next to the small boat basin's entrance. A layer of sediment up to 1 m thick was deposited along the central portion of the entry of the outer boat basin,

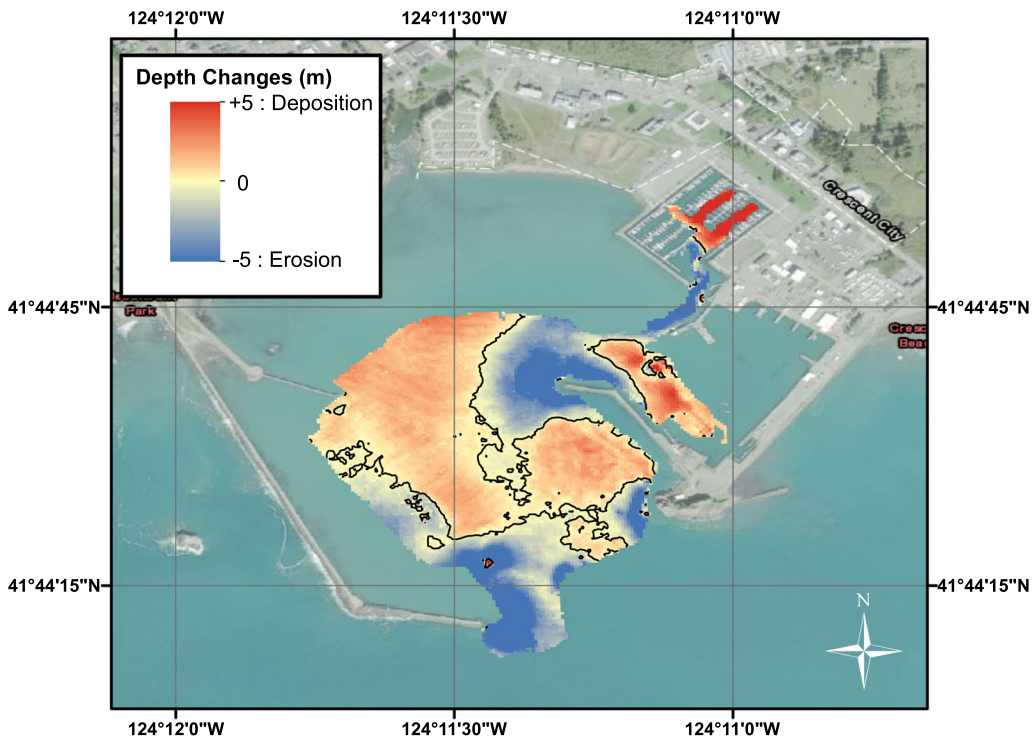

Figure 2
Bed changes inside Crescent City harbor during the 2011 tsunami, determined from the difference of two surveys performed in 2008 (NOAA, 2008) and in March 2011 (NOAA, 2011). (Wilson et al. 2012). Black line depicts contour line of zero bed change

parallel to the scoured zone. The video analysis concluded that current velocities were up to 4.6 m/s near the small boat basin's entrance.

3.1.2 Model Simulations

We simulated the effects of the 2011 tsunami in Crescent City harbor using the tsunami source described in Grilli et al. (2013), who employed a 3D finite element model to model the Tohoku-Oki tsunami source. Details of the source configuration, ocean basin grid, and configuration of the propagation model may be found in Grilli et al. (2013) and Kirby et al. (2013). The additional Submarine Mass Failure (SMF) source described by Tappin et al. (2014) is not included, as its impact on far field results is minimal. A comparison of simulated and measured water surface displacements at DART buoy 46407 is shown in Fig. 3a. The model results are shifted 8 mins backward to compensate for the difference between the tsunami's calculated and measured arrival time. This 8-min difference is probably related to the neglection of compressibility and earth elasticity effects in the ocean-scale simulations (Abdolali and Kirby 2017; Abdolali et al. 2019; Allgeyer and Cummins 2014; Wang 2015).

The ocean-basin simulation results were used as boundary condition input for the local simulation of tsunami conditions inside Crescent City harbor. Calculations were carried out using five levels of one-way nesting to increase the resolution from 16 arc-seconds in the offshore up to 1/6 arc-seconds around the harbor. The bathymetry data for the 16 arc-second grid (Fig. 4) was obtained from Coastal Relief Model (CRM) 3 arc-second data (NGDC, 2003) in nearshore areas, and through interpolation of

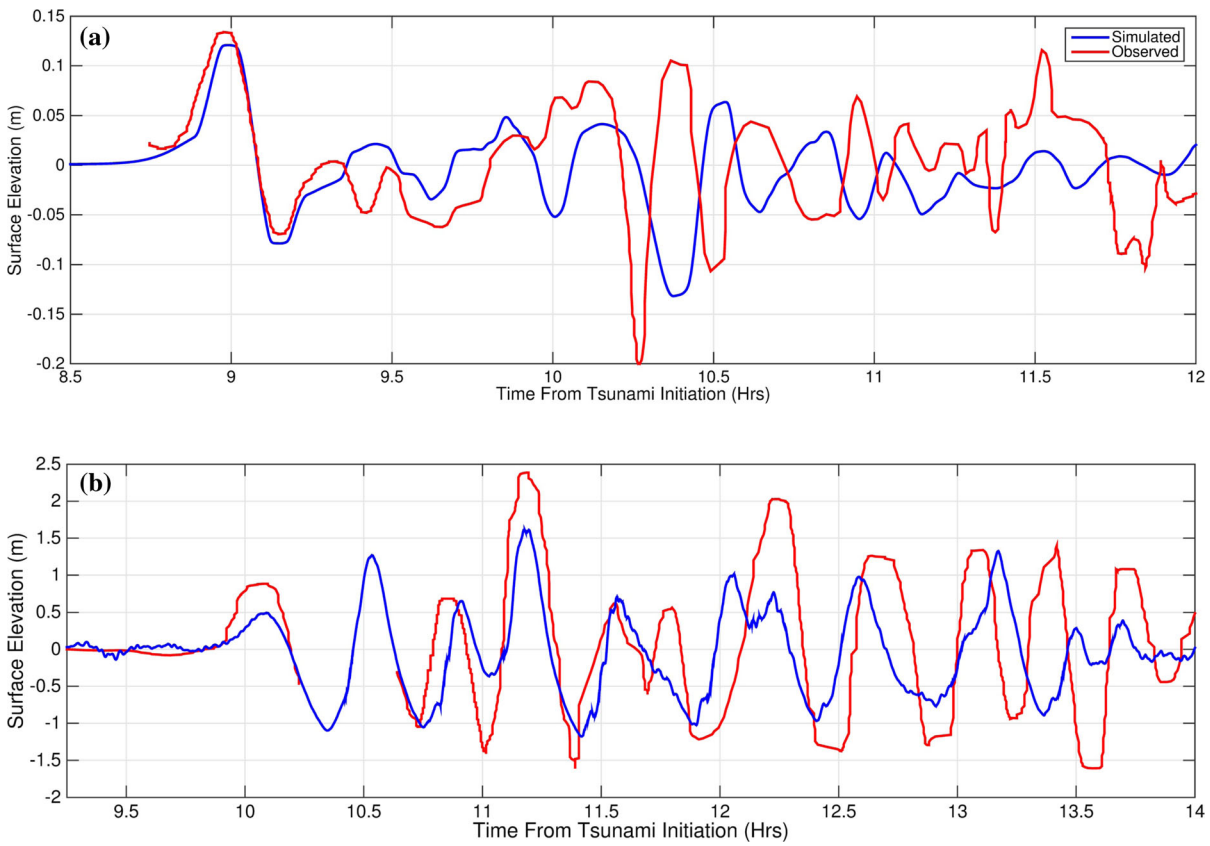

Figure 3
Comparison between measured (red) and calculated (blue) surface elevations during 2011 Tohoku-oki tsunami at **a** DART buoy 46407 and **b** entrance of small boat basin in Crescent City harbor

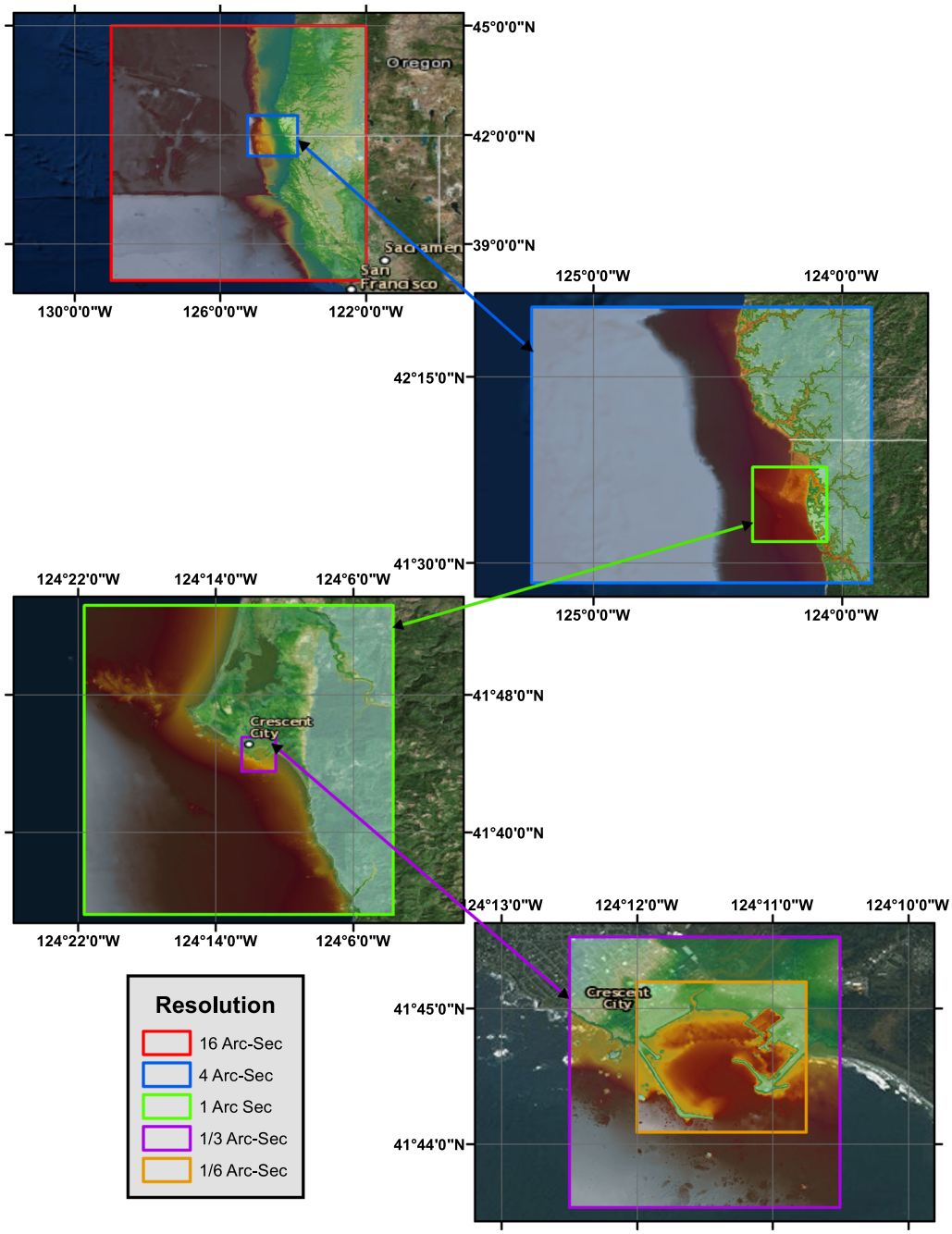

Figure 4
Nesting approach used to model the morphological effects of 2011 Tohoku-Oki Tsunami inside the Crescent City harbour

1 arc-min ETOPO1 data (Amante and Eakins 2009) in areas not covered by CRM data. The flow information of 16 arc-second simulations was recorded around the Crescent City harbor DEM (Grothe et al. 2011) for the 4 arc-second simulations (Fig. 4).

The Crescent City harbor DEM is the data used by Wilson et al. (2012) as their pre-tsunami bathymetry,

and has 1/3 arc-second resolution and was the bathymetry source used to construct 4, 1, 1/3 and 1/6 arc-second grids. The bathymetry data for 1/6 arc-second grid was obtained through linear interpolation of the original 1/3 arc-second data. Also, knowing that the tsunami reached the Crescent City at low tide conditions, we converted the DEM's vertical datum from Mean High Water (MHW) to Mean Low Water (MLW). Figure 5 shows the computational domain of 1/6 arc-second simulation grid used to model morphological changes during 2011 tsunami inside the Crescent City harbor. The grid dimension is 450 $\times$ 400 in x and y directions, with $\Delta x = 3.83$ m and $\Delta y = 5.15$ m corresponding to 1/6 arc-second at the Crescent City latitude.

Figure 6 illustrates the sandy regions inside the harbor. Wilson et al. (2012) reported that deposited sediments were mostly fine sand and silt, mainly from the inside of the harbor. Therefore, the median grain size was assumed to be 0.2 mm, with 2.0 cm/s fall velocity. Tests with grain sizes varying in a range of 0.1–0.4 mm showed negligible variations in the final results. The angle of repose of the sediment used in the avalanching scheme was set to be $\tan(\phi) = 0.5$, and the porosity coefficient is taken to be 0.4.

During simulations using a uniform drag coefficient for the whole domain, we noticed that some of the jetties were inundated and over-topped in disagreement with reported observations. Thus, to address this issue, we used different drag coefficients for harbor structures compared to sandy regions. For jetties, breakwaters, and rocky regions we used the drag coefficient of $C_d = 0.1$, and for the sandy bottom, the $C_d = 0.005$ was used corresponding to the sediment grain size. We observed that defining large drag coefficients for coastal structures improved the results significantly, especially around the jetties where large scours occurred. Using a combination of GIS work and calculation of bed slope, we distinguished the sandy regions of the harbor from hard bottom areas. We assumed that the areas with slopes

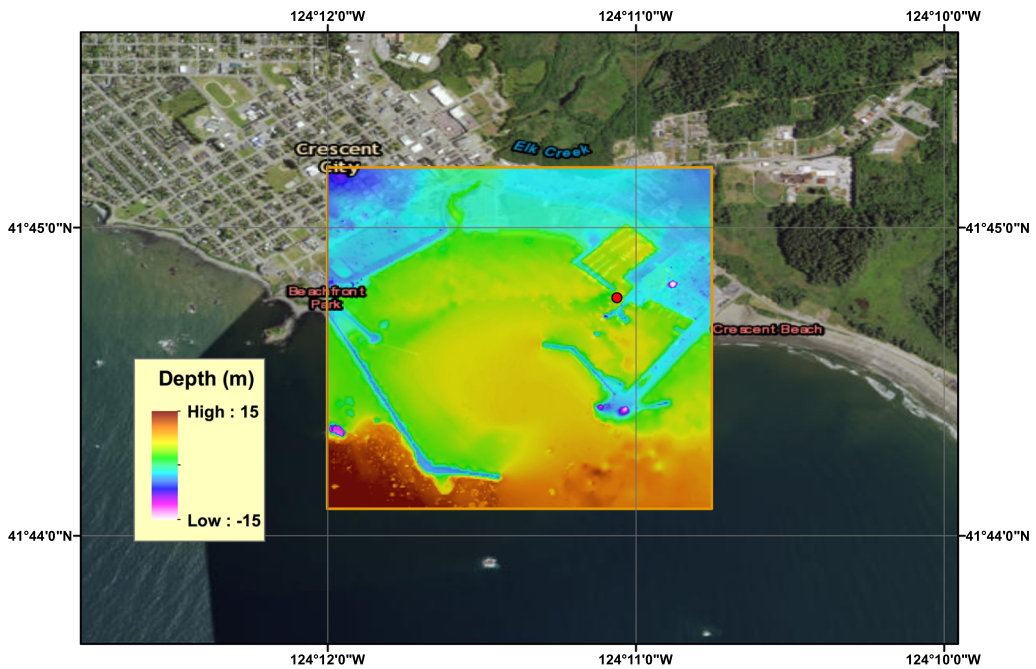

Figure 5
Computational domain of 1/6 arc-second grid used for modeling tsunami-induced morphological changes inside the Crescent City harbor. The red circle shows the location of the tide gauge inside the harbor

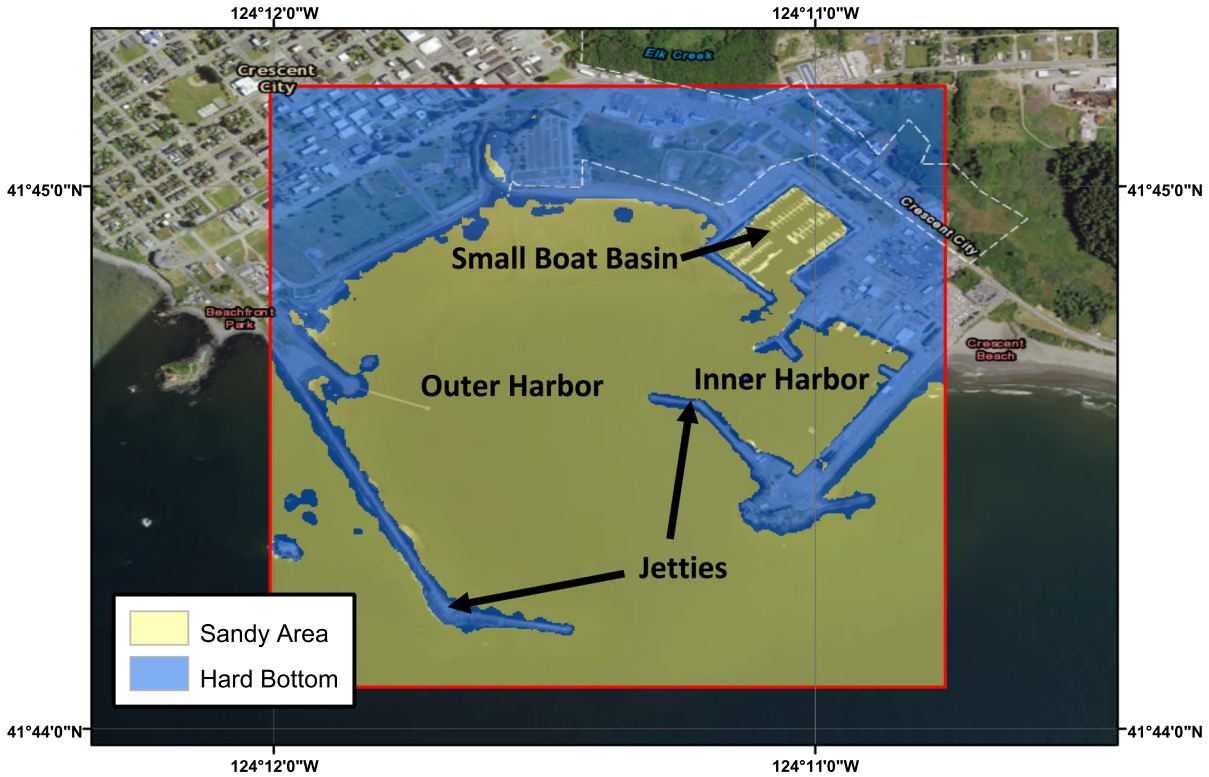

Figure 6
Hard bottom areas defined in the model for simulation of sediment transport during the 2011 tsunami inside the Crescent City harbor (Blue regions)

larger than 0.5 were either rocky points or coastal structure regions.

3.1.3 Results

Figure 3b shows the comparison between calculated and measured surface elevations in the entrance of small boat basin (Fig. 6). The location of the gauge is depicted in Fig. 5. Tide gauge data in the boat basin is not available for the period of 10.2–10.7 h after the initial tsunami event. This time span includes the arrival of the first tsunami wave. Overall, model results show good agreement with recorded data, although the model underestimates the largest crest elevations of the tsunami signal in the small boat basin entrance. The model also underestimates the effect of trapped wave resonance around the harbor due to the small size of the nested grid (Horrillo et al. 2008).

Wilson et al. (2012) reported that the dominant process causing bed changes in the small boat basin entrance was the outflow-inflow regime caused by 2011 tsunami inside the harbor. The agreement between the frequency of measured and calculated surface elevation shows that the model could capture the inflow-outflow regime correctly. Lee et al. (2012) reported that at low tide conditions the resonant wave period in the harbor is 20 mins, through spectral analysis of 2011 Japan and 2010 Chile tsunami signals in Crescent City harbor. They used idealized cases to calculate the resonance of the harbor during different tide conditions, where large waves were propagated toward the harbor, and the following perturbation frequency was considered to be the natural frequency of the harbor. They used the mild-slope equation to model the response curves at the tide gauge in Crescent City, and showed that the resonance period for the harbor is 20 mins at low tide.

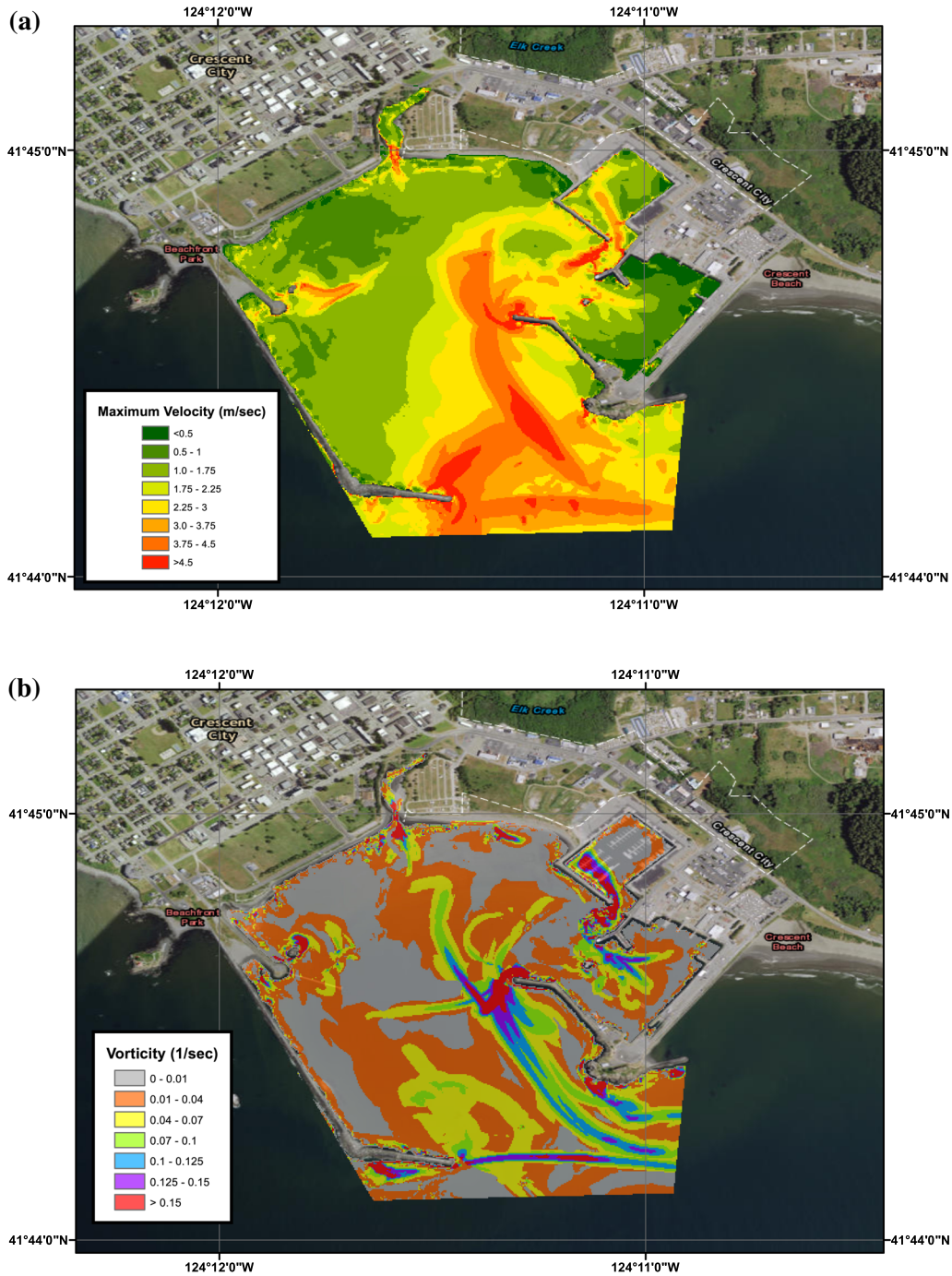

Figure 7
Maximum computed **a** velocity and **b** vertical vorticity inside Crescent City harbor for 2011 Japan tsunami

The 20 min period is comparable to measured and computed results shown in Fig. 3b.

The maximum velocity and vorticity calculated by the model inside the Crescent City harbor shown in Fig. 7a, b. The largest velocities were recorded along the navigation channel, where the deepest parts of the inner harbor are located. Wilson et al. (2012) concluded that the inflow-outflow velocity in the

entrance channel of the small boat basin was 4.5 m/s, and about 3.0 m/s inside the small boat basin, similar to the values calculated by the model. The model also estimated large velocities with a similar order of magnitude close to the jetties in the inner and outer harbor, correlating to the location of largest erosion observed in the harbor after the tsunami. The largest values of vorticity and velocity mostly were located at similar locations inside the harbor, although vorticity was large close to the structures even in areas where large velocities are not calculated. The largest vortices are located close to the jetty in the inner harbor and the entrance of the small boat basin as well as along navigation channels.

Computed bed changes are shown in Fig. 8. The model results show significant erosion near the jetties in the entrance of the harbor, similar to the field observations. The areas with significant erosion correspond with areas where the model calculated large vertical vorticity or high velocities (Fig. 7). The largest erosion depths were calculated on the back side of the jetty in the mid harbor entrance and along the mouth of the small boat basin, with erosions between 2 and 3 m. Also, the model calculated a significant amount of sediment deposition inside the boat basins in the low current velocity regime, parallel to observations. Wilson et al. (2012) reported that the deposition inside the boat basin was significant, rendering it unnavigable after the tsunami. The model computed accretion of a sediment layer with a thickness between 0.75 and 2 m in both of the boat basins.

Figure 9 compares measured and calculated erosion-deposition patterns inside Crescent City harbor after the 2011 tsunami. The results are generally in good agreement with field observations, where erosions were computed near the jetties and at the mouth of the small boat basin. Also, the model computed accretion of sediment in the middle of the outer harbor and inside the boat basins. The similarity between modeled and measured erosion-deposition patterns shows that the model is capable of locating erosion or deposition correctly. However, there are some differences between the bed change values, especially for the maximum erosion calculated by the model in comparison to the observations.

The model was able to capture the general trend of morphological change inside Crescent City harbor, although larger erosions were observed in field surveys. The model computed a maximum erosion depth of 2.5 m around the jetties, where the measured scour holes were almost 5.5 m deep. Also, the erosion in the entrance channel of the small boat basin is underestimated by 2 m in the model, compared to observed 5.5 m. Two main reasons could be the cause of this difference between model results and field observations. First, because of the resolution of the grid used for simulations, the scour holes are not allowed to grow larger than a value determined by the avalanching limit (repose angle of sediment), which forces the slope to be the maximum value of 0.5. Although the avalanching scheme is constrained by the grid size, it is a vital part of the bed evolution simulation process and the results in its absence would be inaccurate. Secondly, the underestimation of significant erosions could be the shorter tsunami duration captured by the model compared to the observations. Wilson et al. (2012) reported that the tsunami signal lasted for 3 days in Crescent City harbor, with the inflow-outflow regime constantly changing the harbor bed. However, the model only captures 6 h of the event. This could be because of convergence issues for the ocean-basin simulation where the reflective waves that generate the edge waves are not captured properly. During our simulations, we observed that each inflow-outflow occurrence resulted in a similar pattern of erosion-deposition shown in Fig. 9, with the values of accretion and scour increasing, but the erosion-deposition pattern stayed constant after the first inflow-outflow event. Thus, if the model could have captured the duration of the tsunami correctly, probably better estimates of the erosion depths would have been achieved. This is also reflected in the total volume of computed erosion and deposition volumes inside the harbor. Overall, the model computed about 95,000 m^3 of erosion and 65,000 m^3 deposition inside the harbor, with the residual sediment either deposited outside the harbor or forced out of the computational domain boundaries. The total computed deposition and erosion volumes are about one-third of the measured values reported by Wilson et al. (2012). Considering the similar erosion-deposition

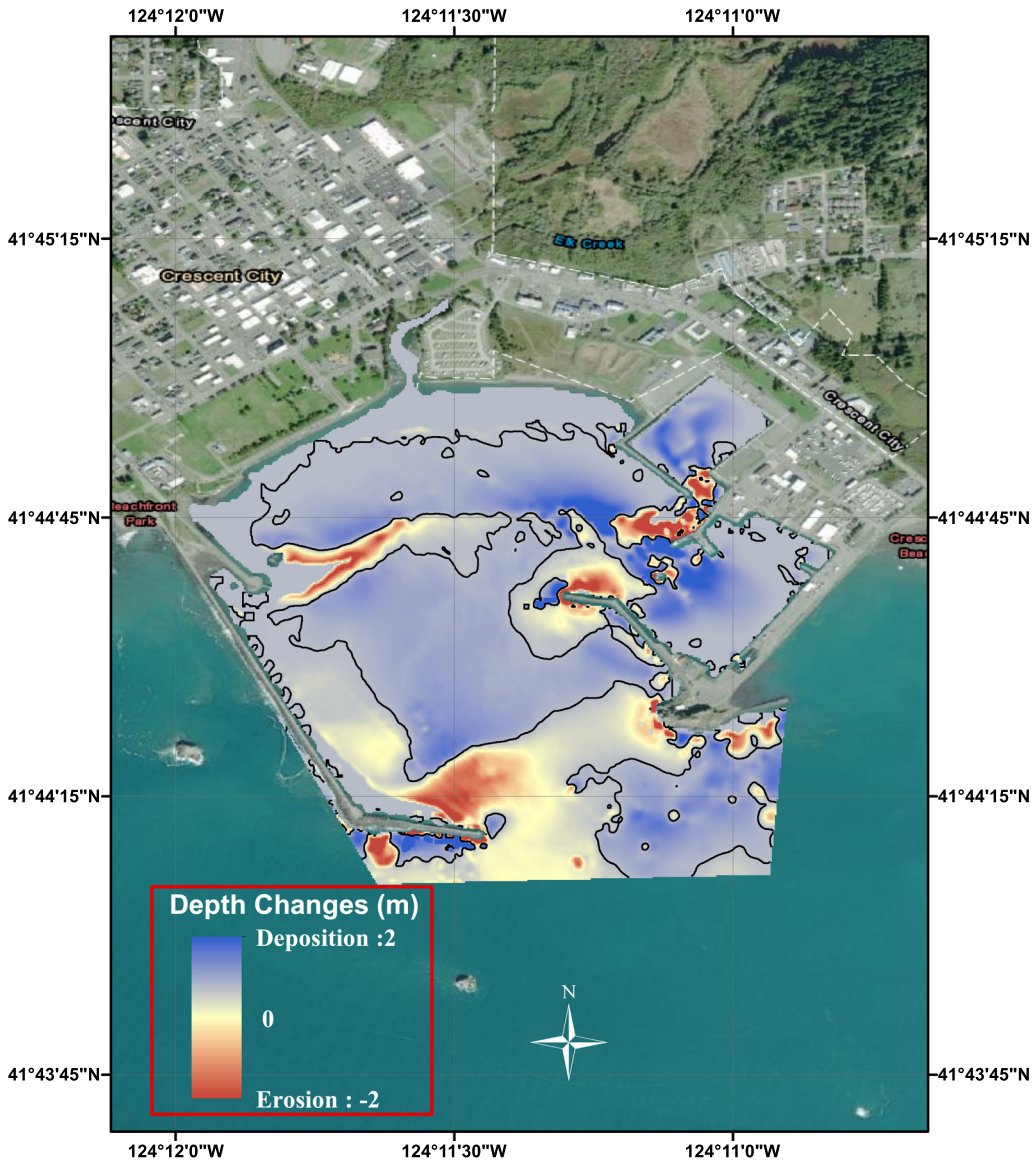

Figure 8
Computed bed changes in Crescent City harbor during 2011 Tohoku-Oki Tsunami. Green, blue, purple and white colors represent the eroded areas. Black line depicts contour line of zero bed change

pattern of measured and simulated bed changes (Fig. 9), the differences between erosion and deposition volumes are mainly because of the differences between the captured and actual time scale of the event. Moreover, ignoring the 3D effects through using a depth-averaged model could be another reason for the difference between computed and measured bed changes.

Overall, the model successfully computed the erosion-deposition pattern inside Crescent City harbor during the 2011 tsunami. Although some differences exist between model results and field observations, mainly the magnitude of the largest scours around the jetties, the outcome shows that the model is capable of simulating tsunami-induced morphological change over complex bathymetry

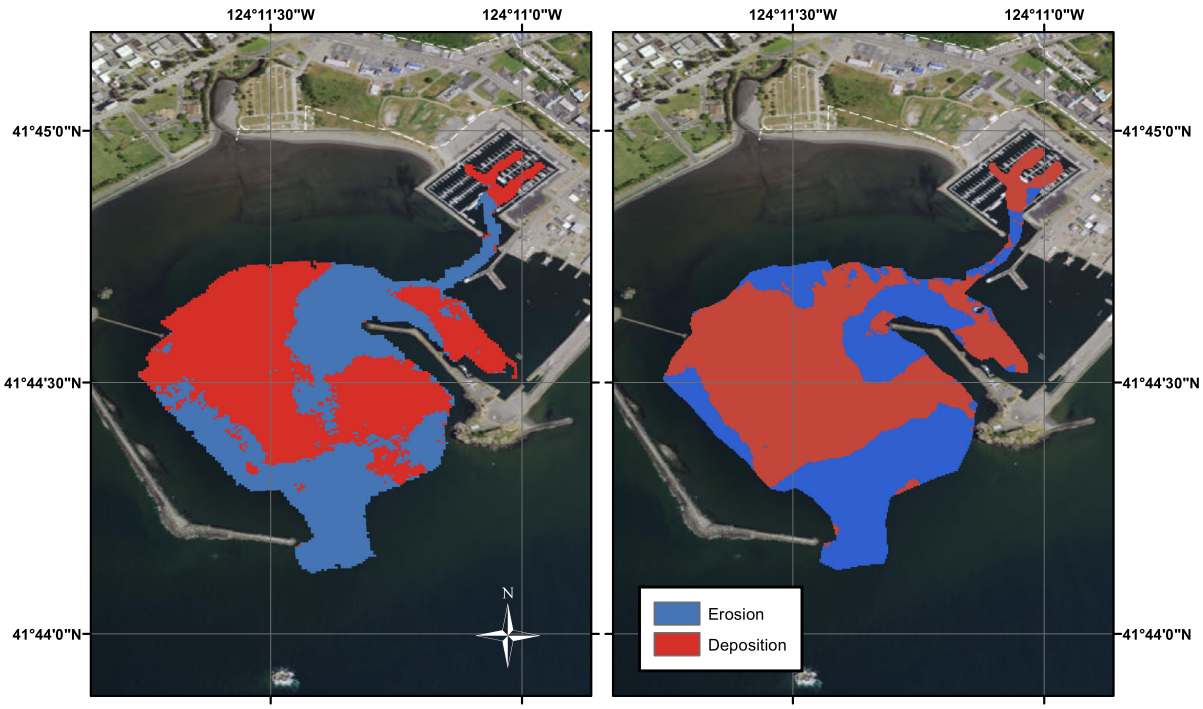

Figure 9
Erosion-deposition pattern inside the Crescent City harbor after 2011 tsunami; measured (left), computed (right). In both figures the blue color represents erosion and red color show deposition

and in proximity to structures and hard bottom regions.

4. *Barrier Island Response to Tsunami Inundation: Assateague Island, MD USA*

In this section, we provide a hypothetical estimate of effects of tsunamis on an erodible barrier island. Topography for this example corresponds to a section of Assateague Island, MD, USA, south of Ocean City, MD and contained with the Ocean City tsunami DEM (Grothe et al. 2010), shown in Fig. 10. First generation inundation mapping has been carried out for the northern portion of the area based on four tsunami sources, including two seismic sources [a $M_w = 9.0$ earthquake in Puerto Rico (PR) trench zone in the Caribbean Subduction Zone (Grilli et al. 2010) and the historic Azores Convergence Zone earthquake of 1755 (Lander et al. 1993)] near Lisbon, Portugal, a far-field subaerial landslide due to a volcanic collapse of Cumbre Vieja Volcano (CVV) in the Canary Islands (Tehranirad et al. 2015a), and a near-field Submarine Mass Failures (SMFs) close to the edge of the US East Coast continental shelf (Grilli et al. 2015). Construction and layout of grids for the region and the process of one-way nesting to move information from larger to smaller scales, are described in Tehranirad et al. (2014). The present simulations are identical to previous calculations up to the final grid refinement, where the morphology model is utilized instead of the purely hydrodynamic simulations described previously. Tsunami inundation for Assateague Island was modeled with 1/3 arcsec resolution. Figure 11 illustrates the nesting approach used in this study to model different tsunamis on Assateague Island and Ocean City.

Fenster et al. (2016) measured sediment grain size distribution along the southern Maryland and Virgina barrier islands. They reported that for Assateague Island, the median grain size (d_{50}) is 0.36 ± 0.09 mm. We used the reported median grain size with computed fall velocity of $w_f = 2.0$ cm/s (2) and maximum bed slope $\tan\phi = 0.5$, to be used in the

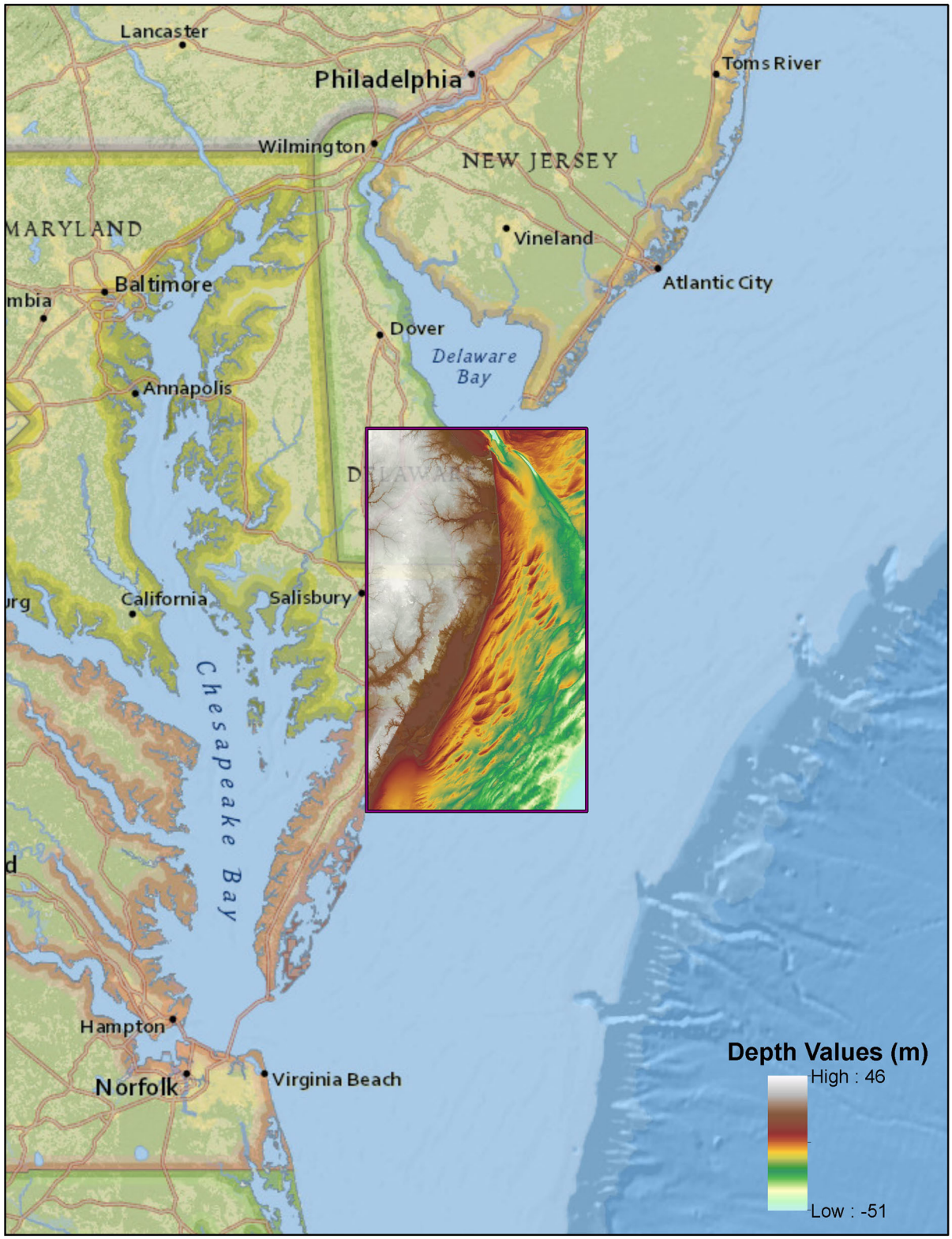

Figure 10
Area covered by the Ocean City DEM. Color bar shows depth values in meters for areas inside of the DEM boundary

avalanching scheme. We assumed that the study area is entirely covered by sand with no pavement and no vegetation. A Manning coefficient of $n = 0.025$ was used during simulations, following the values that Sugawara et al. (2014b) provided for a similar environment. The porosity was assumed to be the standard value of 0.4. The time step Δt varied between 0.07 and 0.3 s during the simulations. The ratio of morphology time step over hydrodynamics time step ($\Delta t_{morph}/\Delta t$) was set to be 20. Figure 12 shows time series of surface elevation data recorded at the southeastern edge of 1/3 arc-sec Assateague Island grid for each of the sources considered.

4.1. *Assateague Island Morphological Response to Tsunami Inundation*

Computations of the tsunami-induced morphological change on Assateague Island were carried out using the computational domain shown in the bottom left of Fig. 10. The domain grid size was 810 × 810 with 1/3 arc-sec resolution, corresponding to $\Delta x = 8.10$ m and $\Delta y = 10.27$ m, extracted from the Ocean City DEM. Surface elevations and velocity terms (u, v) were forced on the boundaries using information recorded during the 1 arc-sec simulations for CVV, Lisbon, PRT, and SMF sources.

A morphological process similar to that of the first wave keeps happening for several successive waves during the time between 20 and 120 mins of simulating nearshore effects of CVV tsunami on Assateague Island. This process can be divided into two steps. First, the tsunami wave overtops the barrier, erodes the top and back of the island and deposits sand in the back bay. Next, during rundown, the shoreface on both sides of the barrier and the front dune gets significantly eroded, and the sediment gets deposited offshore, both in the ocean and the back bay. Consequently, the next wave reaching the shoreline faces a smoother bathymetry, flattened by previous waves.

Two hours after the first wave of the CVV tsunami reached the shoreline, a significant volume of water was trapped in the bay between the barrier island and the mainland behind it. This causes a gradient between water surface elevations on two sides of the barrier island, where the back bay water surface is about 2–5 m higher than that of the ocean. Therefore, because of this hydraulic head, the trapped water between the barrier and the mainland starts to pour back into the ocean, causing substantial morphological changes. The water flows back into the ocean continuously for 3–4 h, almost in quasi-uniform condition with velocities in order of 0.2–0.5 m/s. Although some of the residual waves in the tsunami signal overtop the barrier during this time, the flow regime is mainly directed offshore when the water surface on the back bay is higher than the ocean. This continuous flow regime moves the sediment offshore. In the bay, the sediment gets accumulated behind the original shoreline on the back side of the barrier, where was previously deposited during the overtopping process. Moreover, the shoreface and the front dune get heavily scoured, and their corresponding sediment deposited offshore. Udo et al. (2016) reported a similar pattern after the 2011 Tohuku-Oki tsunami on the coast of Rikuzen-Takata Coast.

The computed results for other tsunami sources showed a similar morphological response for the Assateague Island during tsunami inundation compared to the CVV source. Figure 13 depicts the computed bed level changes for all of the sources studied in this work for a typical cross-section of the island. The calculated results for the PR and SMF sources show significant bed changes on top of the barrier similar to the CVV tsunami. However, the Lisbon tsunami, which has much smaller waves compared to three other sources (Fig. 12) did not overtop the Assateague Island barrier and correspondingly did not cause any notable change to the topography of the study area.

Figure 14a–d show the computed bed changes of Assateague Island during simulations of PR, Lisbon, CVV and SMF tsunami sources. Bed changes less than 20 cm are filtered out of these figures for clarity. Significant tsunamis (PR, CVV and SMF) changed the coastal morphology in a similar manner. The shoreface and the front dune of the barrier island got eroded, and the moved sand got deposited either in the back bay or offshore in the ocean. However, in contrast to the large tsunami sources, the Lisbon tsunami does not effectively over-top the Assateague Island barrier in a way to create notable changes on

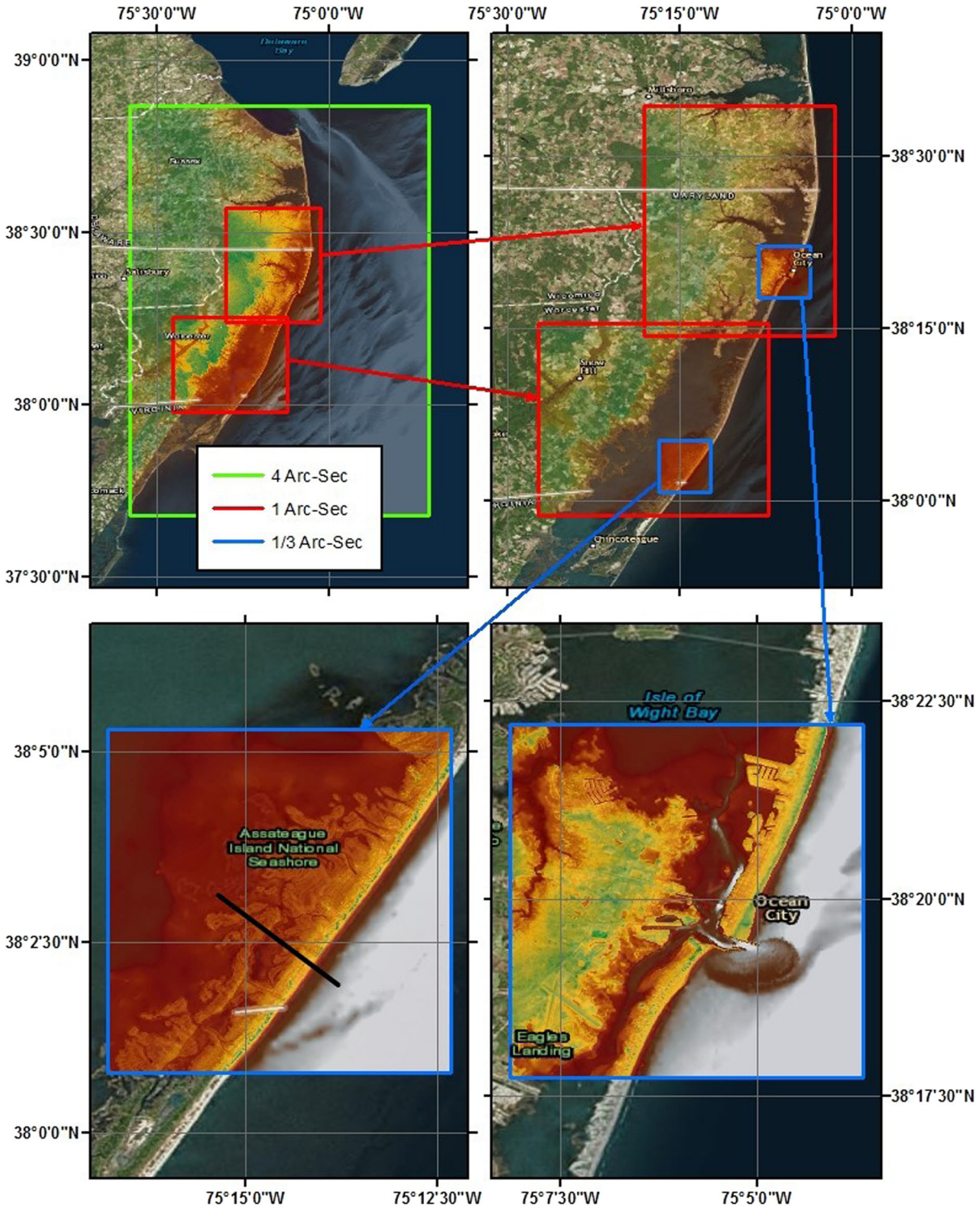
75°30'0"W
75°0'0"W
75°30'0"W
75°15'0"W
75°0'0"W
39°0'0"N
38°30'0"N
38°0'0"N
37°30'0"N
38°15'0"N
4 Arc-Sec
1 Arc-Sec
1/3 Arc-Sec
Salisbury
Wallops
Ocean City
Chincoteague
38°5'0"N
38°2'30"N
38°22'30"N
38°20'0"N
38°17'30"N
Assateague Island National Seashore
Isle of Wight Bay
Eagles Landing
75°15'0"W
75°12'30"W
75°7'30"W
75°5'0"W

◀Figure 11
Nesting approach used to model tsunami morphological effects in Assateague Island (Bottom-Left), and Ocean City (Bottom-Right). Computations were performed using 4, 1 and 1/3 arc-second resolution grids, which are depicted with different colors. Black line shows the cross-section shown in Fig. 13

the coastal morphology. The computed bed changes for the CVV is larger than other sources, regarding its magnitude compared to PR and SMF tsunamis. The computed bed changes for PR and SMF tsunamis are comparable to each other, with PR source causing larger erosions on the shoreface.

Figure 15 illustrates the change in extent of the island's subaerial topography for the PR and CVV events. Except for the Lisbon tsunami, results suggest that, during a significant tsunami, the barrier island planform moves onshore due to overwash processes. The barrier island migration onshore mainly occurs due to two processes. First, during the time that tsunami overtops the barrier island significant erosion on the top and lee side of the barrier island occurs and the eroded sand deposits in the back bay. Second, during tsunami rundown seaside of the barrier island gets eroded, and the eroded sand deposits offshore. The shoreface also gets eroded while the trapped water between the mainland and the barrier flows

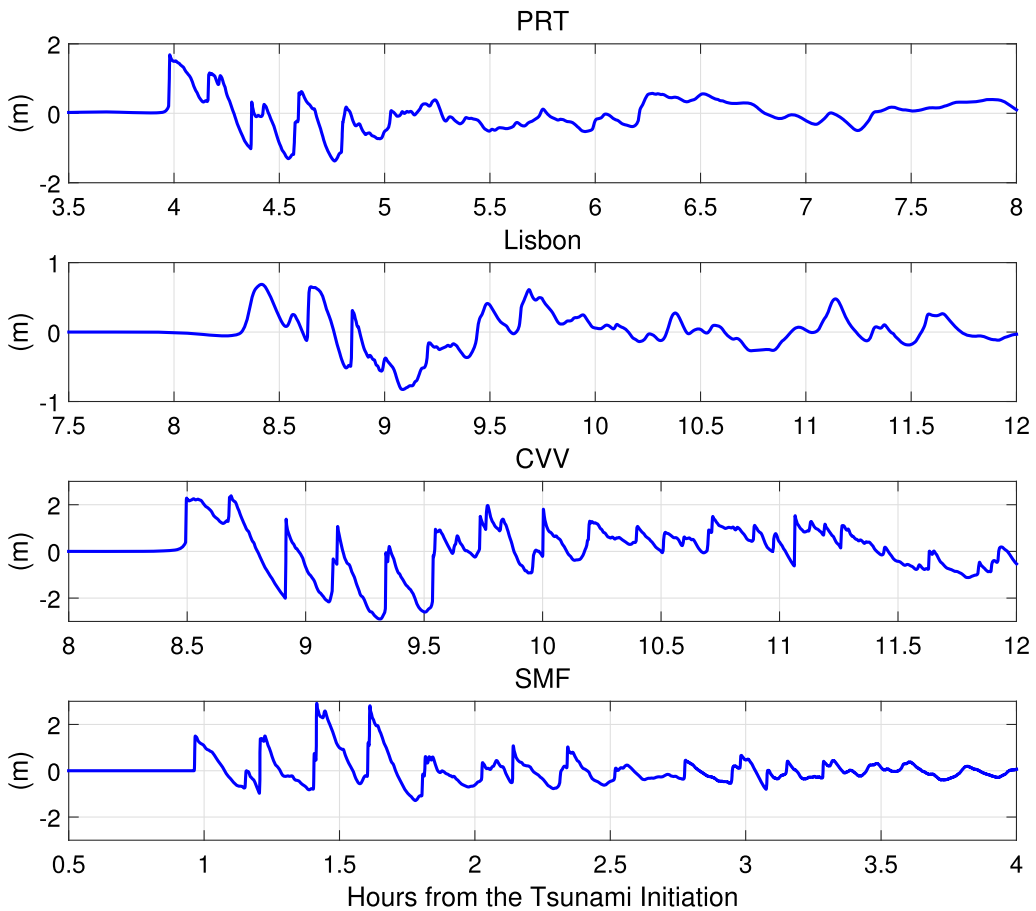

Figure 12
Surface elevation at the southeastern edge of the 1/3 arc-sec Assateague Island computational domain (bottom-left of Fig. 10) for all of the tsunami sources studied in this work

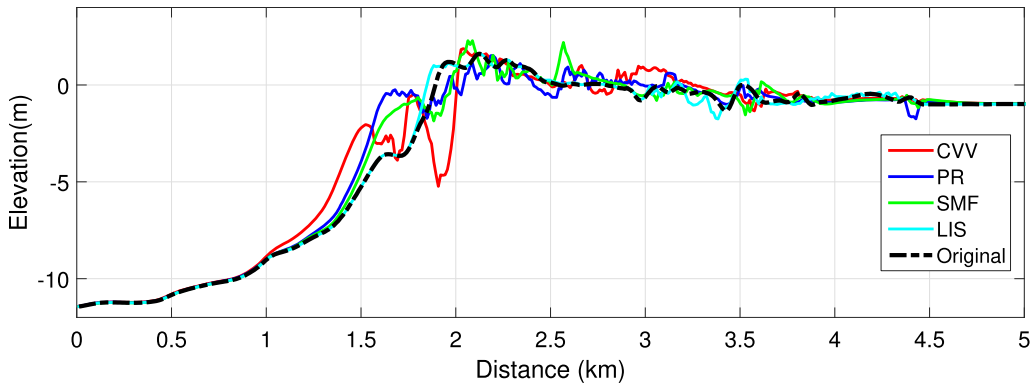

Figure 13
Computed bed elevation changes on a cross-section for the CVV, PRT, SMF and Lisbon tsunami sources. The location of cross-section is shown in Fig. 11

back into the ocean. In the aftermath of sand deposition in the back bay and erosion on the shoreface, barrier island emerges from water further onshore, with much flatter topography compared to pre-tsunami bathymetry.

5. *Discussion and Conclusions*

A morphology model for tsunami-induced sediment transport has been developed based on a well-tested Boussinesq model code FUNWAVE-TVD. The model has been shown to perform satisfactorily in comparison to laboratory (Tehranirad et al. 2016, 2017) and field cases, and has been used in a speculative example of barrier island reworking by incident tsunami waves. Several aspects of the simulations deserve further discussion, and are addressed here. This model's sensitivity to different types of vegetation, porosity, and avalanching are other factors that require further investigation in the future.

5.1. *Plug Flow Instability*

Tsunami flow is considered to be quasi-steady for most of the inundation process (Jaffe and Gelfenbaum 2007; Sugawara et al. 2014b), since the temporal gradients in mean flow speed are insignificant when averaged over the period of turbulent fluctuations during most of the tsunami inundation. However, near the leading edge of the advancing tsunami wave, plug flow might form because of high flow acceleration. Plug flow is a type of bed instability created under high flow acceleration (Sleath 1999), which could result in significant bed destabilization and erosion. In order to evaluate the potential for this effect to affect the overall calculations, we studied calculated flow accelerations obtained from inundation simulations of an SMF tsunami in Atlantic City, NJ (Tehranirad et al. 2015b). Figure 16 shows nearshore flow properties for the chosen SMF tsunami. Except for a few spikes, the flow acceleration is on the order of 0.001 m/s^2, and the acceleration averaged over 1 min (which is much smaller than the average period of flow fluctuations of a tsunami) has a maximum value of about 0.1 m/s^2. Based on these numbers, it can be concluded that the assumption of quasi-steady flow for a tsunami is appropriate. To further address the plug flow question, we calculated the Sleath parameter at the same location used for flow condition analysis (Fig. 16). Foster et al. (2006) provide a description of Sleath parameter based on flow acceleration, given by

$$S(t) = \frac{p_{,x}}{\rho_w (s-1) g} = \frac{Du/Dt}{(s-1)g} \tag{5}$$

where s is the sediment specific gravity. Plug flow happens when $S(t)$ is larger than the critical value of 0.29 (Foster et al. 2006). However, as shown at the bottom of Fig. 16, the Sleath parameter S is almost close to zero for most of the tsunami inundation

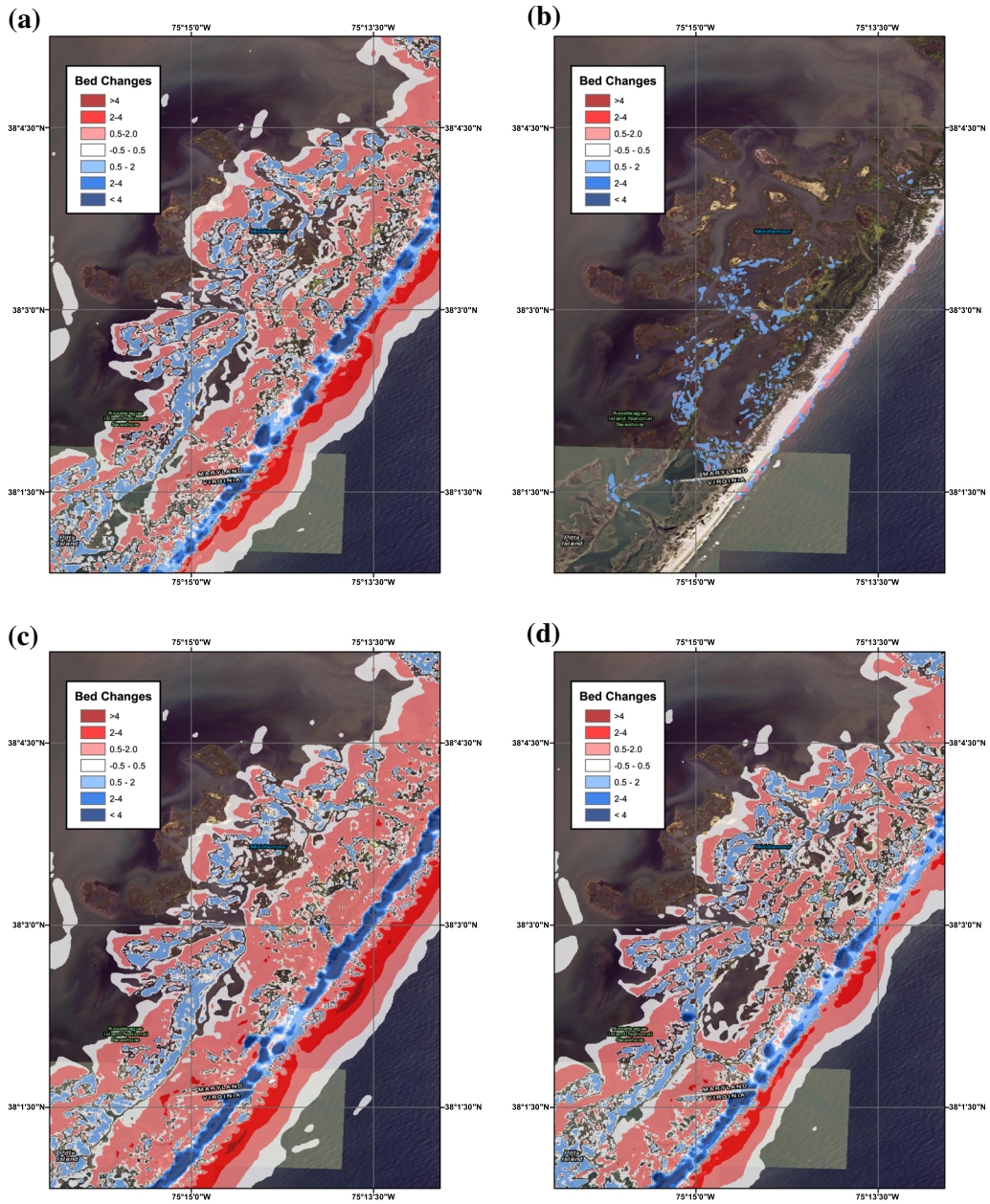

Figure 14
The computed bed changes for Assateague Island during simulations of the **a** PRT, **b** Lisbon, **c** CVV and **d** SMF tsunami sources. Bed changes less than 20 cm are filtered out for clarity. Erosion is represented by blue colors, deposition by red colors

process. Even the spikes close to the bore's front are small. However, Sleath parameter could probably exceed the critical value at the bore front with higher resolution modeling and smaller time steps. To address this problem in our analysis, we looked at the geometrical features of tsunami bore during onshore inundation. The bore front of the tsunami has the surface gradient of about $\partial\eta/\partial x = 1.0$, and it is in order of hundreds of meters long. However, the surface gradient term $\partial\eta/\partial x$ behind bore front is close to

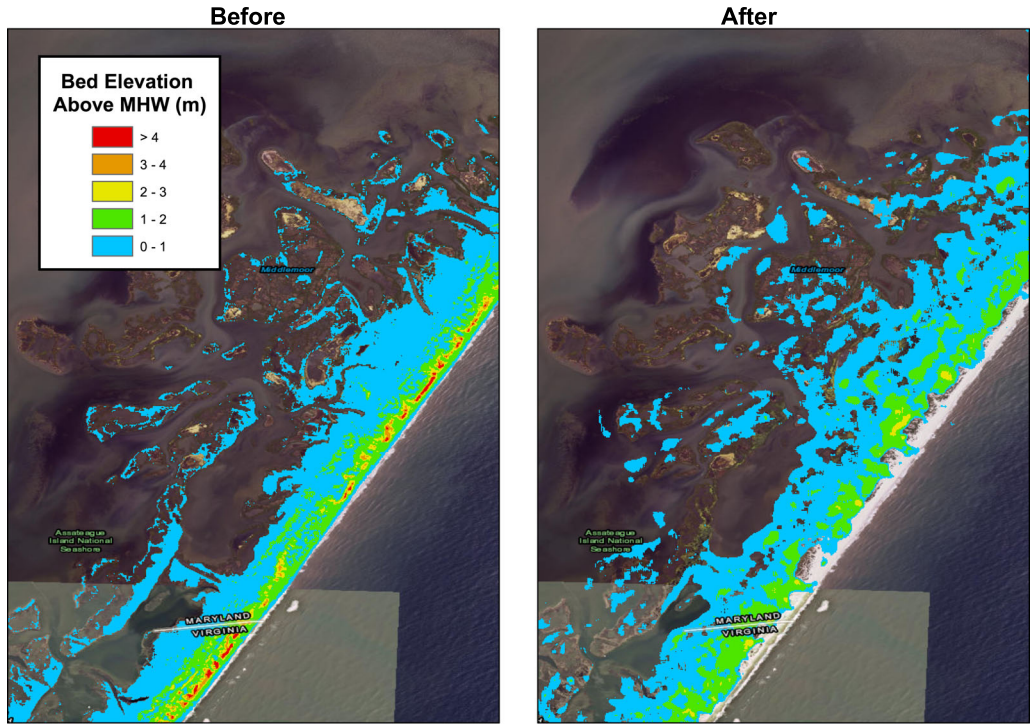

(a)

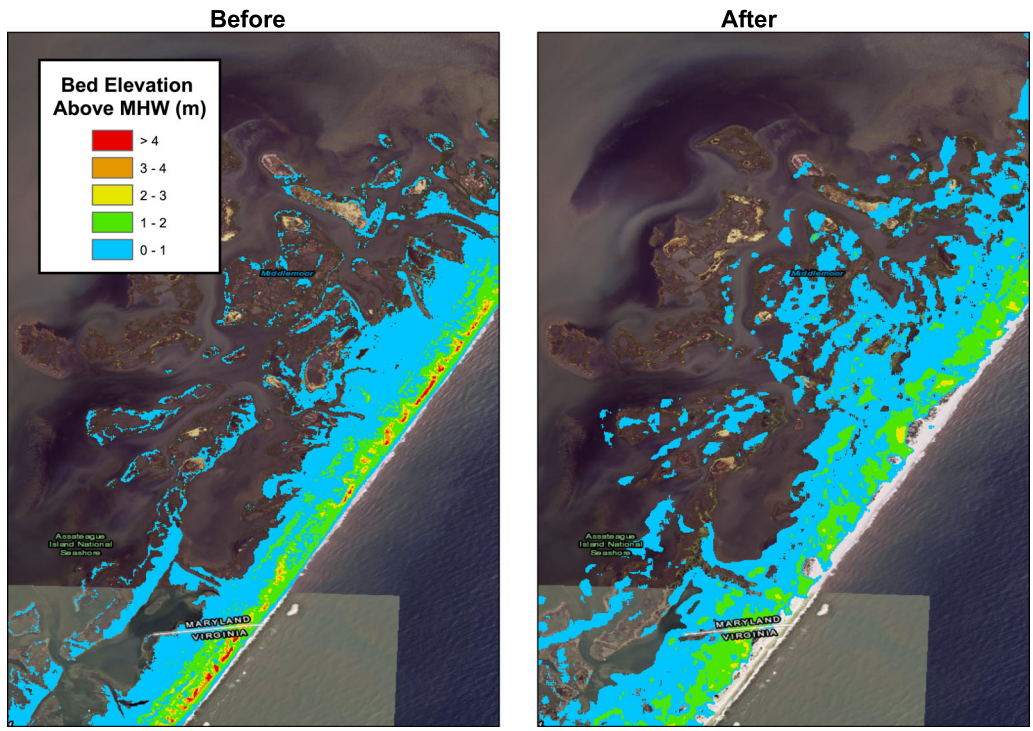

(b)

Figure 15
Subaerial topography of Assateague Island above MHW level before (left) and after (right) the **a** PRT and **b** CVV tsunamis

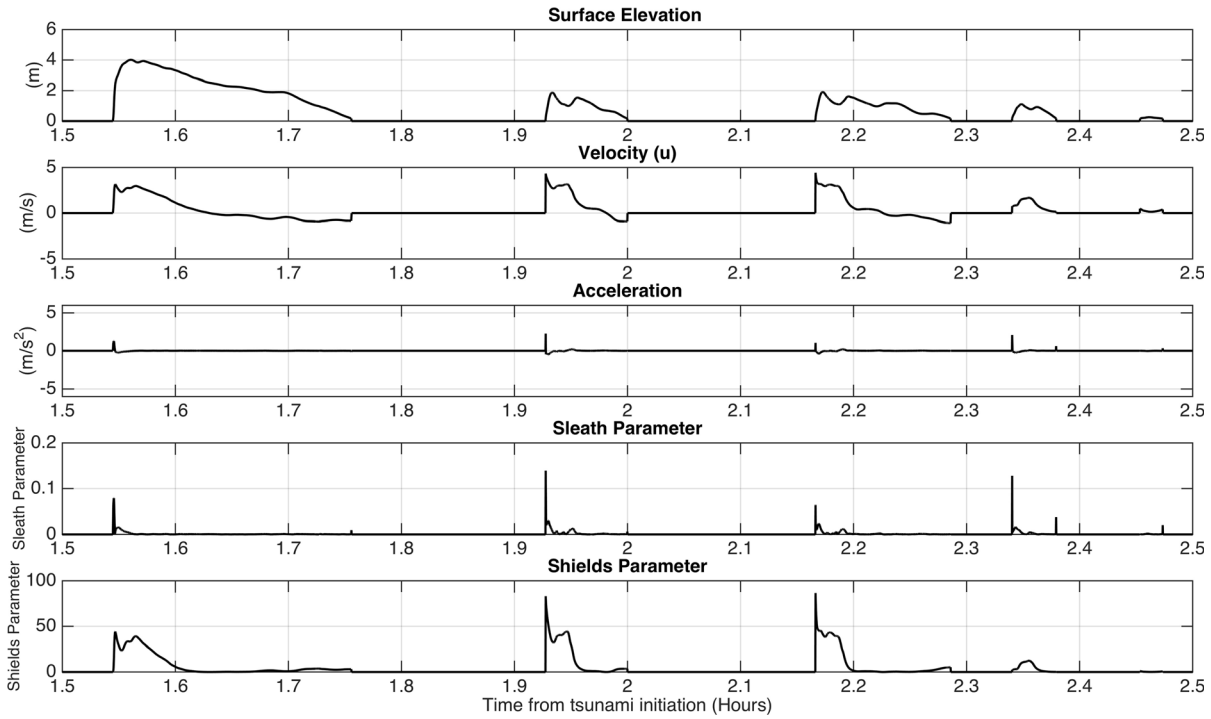

Figure 16
Computed gauge data for a submarine landslide tsunami in an onshore location close to Atlantic City, NJ near the shoreline

zero for a length of several kilometers. Also, considering the hydrostatic approximation for the pressure gradient term ∂_x in the Sleath number estimation (Sleath 1999), one can use the surface gradient term for a rough estimate of Sleath number ($p_{,x} = \rho g \eta_{,x}$). Thus, we can claim that for most of the tsunami bore propagation onshore, the Sleath number is close to zero and for a small portion of the bore front (which is negligible considering the length scale of tsunami waves) plug formation is possible. Accordingly, we decided to neglect bed destabilization caused by plug flow formation.

5.2. Fully-Developed Flow

The estimate of boundary layer thickness ($\delta \sim \sqrt{\nu_t T}$) compared to depth scale of the tsunami in the nearshore shows that quasi-steady assumption for tsunami flow is justifiable. Considering a time scale (T) of about 15 minutes and eddy viscosity of $\nu_t = 10^{-3}$, the boundary layer thickness estimation would be of the order of 1 m, which is similar to the depth scale of the tsunami flow in the nearshore and during onshore inundation. Thus, the boundary layer thickness during most of the tsunami flow onshore extends up to the surface, meaning that the flow would be in fully developed condition, or, in other words, quasi-steady.

5.3. Sheet Flow

Sheet flow is the transport of a high-concentration layer of sediment in the near-bed region and typically occurs when the Shields parameter ($\theta = \tau_b/(\rho g(s-1)d_{50})$) is greater than 1.0 (Sumer et al. 1996). During the inundation process, the Shields parameter exceeds 1.0, and reaches maximum values in the range of 40–75 (Fig. 16), suggesting that sheet flow is occurring, although such bed instabilities were not reported in any of the field observations during tsunami inundation (Goto et al. 2011; Udo et al. 2012; Wilson et al. 2012). However, the focus of the present work was concentrated on establishing a functional model which couples

suspended sediment transport and hydrodynamics during tsunami inundation. Moving forward, the next step should focus on the implementation of the sheet flow transport mode.

5.4. General Model Applicability

Results obtained here indicate that coastal morphology can undergo significant changes during the course of realizable tsunami events. This finding raises the question of whether usual procedures for carrying out tsunami inundation mapping as part of a hazard analysis can lead to an underprediction of the extent of the hazard. The flattening of coastal features such as dunes or berms during the initial stages of a tsunami event could render sheltered areas more vulnerable to attack by subsequent wave crests in a train of tsunami waves. This question is addressed separately in Tehranirad et al. (2017), where the effects of erosion on estimates of tsunami inundation are considered for a US East Coast site.

Acknowledgements

This work has been supported by the US Army Engineers Research and Development Center, contract W912HZ-16-P-0137, and the National Science Foundation Engineering for Natural Hazards program, Grant CMMI-1537232 to the University of Delaware. B. Tehranirad's graduate assistantship was supported by the National Tsunami Hazard Mitigation Program (NOAA) Grants NA10NWS4670010, NA13NWS4670014, NA14NWS4670041 and NA15NWS4670029 to the University of Delaware. Computational resources were provided by Instructional Technology at the University of Delaware. FUNWAVE-TVD may be obtained at http://www.github.com/fengyanshi/FUNWAVE-TVD, with online documentation and released versions at http://fengyanshi. github.io/FUNWAVE-TVD.

Compliance with ethical standards

Conflict of interest The authors declare that they have no conflict of interest.

Appendix A: The Depth-Integrated Model for Suspended Sediment Transport

The 3D Advection-Diffusion (AD) equation for suspended sediment load may be written as

$$c_{,t} + \nabla_h \cdot (\mathbf{u}c) + ((w - w_f)c)_{,z} = \nabla_h \cdot (k\nabla_h c) + (\epsilon c_{,z})_{,z} \tag{6}$$

where c is the sediment concentration, $\mathbf{u}(\mathbf{x}, z, t)$ is the horizontal fluid velocity, $w(\mathbf{x}, z, t)$ is vertical fluid velocity, and k and ϵ are horizontal and vertical diffusion coefficients. The geometry for the problem is described in Fig. 17. The model uses fluid velocities provided by the Boussinesq model. The sediment fall velocity is calculated using Rubey (1933)'s formula,

$$w_f = \sqrt{(s-1)gd_{50}}\left(\sqrt{\frac{2}{3} + \frac{36v^2}{(s-1)gd_{50}^3}} \sqrt{\frac{36v^2}{(s-1)gd_{50}^3}}\right) \tag{7}$$

where S is the specific gravity, d_{50} is the median grain size, and v is the kinematic viscosity. The fall velocity is taken here to be a constant for a sediment with given, uniform properties, but could also vary due to flocculation, sediment size distribution or hindered settling effects. Equation (6) may be integrated over the water column, after which use of Leibnitz' rule and the kinematic boundary conditions for the fluid motion gives

$$\left(\int_{-h}^{\eta} c dz\right)_{,t} + \nabla_h \cdot \left(\int_{-h}^{\eta} \mathbf{u}c dz\right) - \left[w_f c + \epsilon c_{,z}\right]_{-h}^{\eta} - \int_{-h}^{\eta} \nabla_h \cdot (k\nabla_h c) dz = 0 \tag{8}$$

where the expression in square brackets represents the difference of the enclosed expression at the upper and lower boundaries. We define a depth-averaged sediment concentration as

$$\overline{c}(\mathbf{x}, t) = \frac{1}{H}\int_{-h}^{\eta} c(\mathbf{x}, z, t) dz; \quad H = h + \eta \tag{9}$$

Horizontal velocity for the Boussinesq model may be written as

$$\mathbf{u} = \mathbf{u}_\alpha(\mathbf{x}, t) + \mu^2 \mathbf{u}_2(\mathbf{x}, z, t) \tag{10}$$

where $\mathbf{u}_\alpha(\mathbf{x}, t)$ is the dependent velocity variable in the Boussinesq formulation (Chen 2006; Nwogu

1993), and where $\mathbf{u}_2(\mathbf{x}, z, t)$ is the weakly-dispersive correction describing depth dependence for irrotational flow (Chen 2006). We neglect the effect of boundary layers on the computation of depth-averaged quantities; extensions to cover these effects may be found in Kim et al. (2009) and Kim (2015). The resulting expression for horizontal sediment flux $\mathbf{q}_s(\mathbf{x}, t)$ is given by

$$\mathbf{q}_s = \int_{-h}^{\eta} \mathbf{u} c dz \simeq \overline{c} H(\mathbf{u}_\alpha + \overline{\mathbf{u}_2}) = \overline{c}\mathbf{M} \tag{11}$$

where $\mathbf{M}$ is the horizontal fluid volume flux. Sediment flux relative to the upper and lower boundaries may be written as

$$w_f c(\eta) + \epsilon(\eta) c_{,z}(\eta) = 0 \tag{12}$$

$$w_f c(-h) + \epsilon(-h) c_{,z}(-h) = D - P \tag{13}$$

where D and P are deposition and pickup rates. Neglecting possible vertical structure of the horizontal diffusion coefficient k leads to the model Eq. (6). Closure of (6) requires specification of P, D and k. We use the expression

$$k = 5.93 u^* H \tag{14}$$

due to Elder (1959), where u^* is the shear velocity, discussed further below.

Appendix A1: The Equilibrium Suspended Sediment Profile

Neglecting horizontal and temporal variations of the flow field leads to an equation governing the equilibrium vertical concentration profile $c(z)$, given by

$$w_f c + \epsilon c_{,z} = 0 \tag{15}$$

We express $c(z)$ in terms of a reference concentration c_0 obtained at a height z_0 above the bed, or $z = -h + z_0$,

$$c(z) = c_0 G(z); \quad G(z_0) = 1 \tag{16}$$

A depth-uniform mixing coefficient ϵ leads to a logarithmic equilibrium distribution. Van Rijn (1984) suggested a distribution for ϵ for combined currents and short waves. Here, we neglected the short wave-related term, due to the assumption of quasi-steady tsunami flow. Van Rijn (1984) current-related mixing coefficient is given by

$$\begin{aligned} \epsilon &= \epsilon_{max}\left(4(z + \frac{z^2}{h})\right); && 0 < 1 + z/h < 1/2 \\ \epsilon &= \epsilon_{max} = \frac{1}{4}\kappa u^* h; && 1/2 < 1 + z/h < 1 \end{aligned} \tag{17}$$

where $\kappa = 0.4$ is the von Karman constant. We set $b = 2$, leading to a parabolic distribution of ϵ in the lower half of the water column. This form leads to a distribution function $G(z)$ given by

$$G(z) = \mathrm{e}^{-\gamma/z_0} \begin{cases} \mathrm{e}^{\gamma/\zeta}; & 0 \le \zeta \le h/2 \\ \mathrm{e}^{\gamma(2/h)^2(h-\zeta)}; & h/2 \le \zeta \le h \end{cases} \tag{18}$$

where $\zeta = h + z$ is distance above the bed and $\gamma = (w_f/\epsilon_{max})(h/2)^2$. The depth-integrated equilibrium sediment concentration is then given by

$$\overline{c} = \frac{c_0}{H}\int_{z_0}^{H} G(\zeta) d\zeta \tag{19}$$

The shear velocity u_* is given by Van Rijn (1985)

$$u^* = \frac{\kappa}{-1 + \log\left(\frac{30H}{k_s}\right)} U_c \tag{20}$$

where U_c is depth-averaged total velocity ($|\mathbf{u}| = \sqrt{(u^2 + v^2)}$ from (9)), $k_s = 2.5 d_{50}$ is Nikuradse roughness coefficient, and d_{50} is the median grain diameter.

Appendix A2: The Pickup Function P

Li and Huang (2013) have conducted numerical simulations of sediment transport using several pickup functions, and showed that calculated bottom changes using the formulation of Van Rijn (1986) had the least error. We use Van Rijn (1986)'s formulation, given by

$$P = 0.015 \frac{d_{50}}{a}\left(\frac{|\tau_b| - \tau_{cr}}{\tau_{cr}}\right) d_*^{-0.3} w_f \tag{21}$$

where a is a reference elevation and is a function of total depth ($a = 0.01H$), τ_b is the bed shear stress, and τ_{cr} is the critical shear stress. P has the dimension of velocity considering the advection-diffusion equation for non-dimensional sediment concentration ($c = c'/\rho_s$). d_* is dimensionless grain size defined as,

$$d_* = d_{50}\left(\frac{(s-1)g}{\nu^2}\right)^{1/3} \tag{22}$$

where s is the specific gravity of the sediment. The critical bed shear stress τ_{cr} used in (21) is defined as,

$$\tau_{cr} = \rho_w(s-1)gd_{50}\theta_{cr} \tag{23}$$

where θ_{cr} is the critical Shields parameter, approximately equal to 0.05. Based on the roughness estimate, the shear stress is expressed as

$$|\tau_b| = \frac{\rho_w \kappa^2}{(-1+\log(30H/k_s))^2} U_c^2. \tag{24}$$

The pickup rate ($P^k_{i,j}$) is calculated using the formula of Van Rijn (1986) formula (21). The numerical pickup rate calculation is performed using the following definition,

$$P^k_{i,j} = c^k_{0_{i,j}} w_f \tag{25}$$

where c_0 is the reference concentration calculated by following definition,

$$c^k_{0_{i,j}} = R\left(\frac{d_{50}}{0.01H_{i,j}}\right)c_b \tag{26}$$

where d_{50} is median grain size and

$$c_b = 0.015\left(\frac{\tau^k_{b_{i,j}} - \tau_{cr}}{\tau_{cr}}\right)^{1.5} d_*^{-0.3} \tag{27}$$

where τ_{cr} is critical shear stress (23) and d_* is dimensionless grain size. R is a reduction factor introduced by Buttolph et al. (2006) to avoid overestimation of pickup rate under strong shear stresses, and is defined as follows,

$$R = \min\left(1.0, \frac{0.65}{c_b}\right) \tag{28}$$

where the bottom shear stress used in (27) is given by

$$\tau^k_{b_{i,j}} = \frac{\rho_w \kappa^2}{\left(-1+\ln(k_s/30H^k_{i,j})\right)^2}\left(U^k_{c_{i,j}}\right)^2 \tag{29}$$

where $k_s = 2.5d_{50}$ is Nikuradse bottom roughness and $\kappa = 0.4$ is von Karman constant.

Appendix A3: Deposition Rate D

The simplest estimate for the deposition rate D would be based on the reference sediment concentration close to the bed and the sediment fall velocity, $D = c_0 w_f$. However, this method overpredicts deposition rates in small depths close to the shoreline. Here, we use the formulation of Cao (1999), given by

$$D = \gamma\bar{c}w_f(1-\gamma\bar{c})^{m_0} \tag{30}$$

where $\gamma = \min[2, (1-n)/\bar{c}]$, n is sediment porosity, and m_0 is a constant given by 2. Cao (1999) obtained this formula using laboratory data (mostly dam-break tests) for calibration.

Appendix A4: Numerical Implementation

The general approach to numerical implementation of the hydrodynamic model FUNWAVE-TVD may be found in Shi et al. (2012). The sediment transport and bed level change calculations described here are implemented as a morphology module within the FUNWAVE-TVD code. Figure 17 shows a flow chart for FUNWAVE-TVD, with additions made to the code to integrate sediment transport and morphology modules shown in red boxes.

Following the structure of FUNWAVE-TVD, we use a finite volume approach to discritize the spatial structure of (6) on a Cartesian grid (Fig. 18), using the MUSCL-TVD scheme and the HLL approximate Riemann solver. The scheme can be chosen to have 2nd or 4th-order accuracy in space. A third-order Stability-Preserving (SSP) Runge-Kutta scheme is used to march (6) and (7) forward in time. Details of the implementation may be found in Tehranirad et al. (2016) and are given schematically here.

The AD equation (6) is written in nearly conservative form as

$$\Psi_{,t} + \nabla_h \cdot \mathbf{F}(\Psi) = S \tag{31}$$

where Ψ and $F(\Psi)$ represent the conserved sediment volume

$$\Psi = \bar{c}H \tag{32}$$

and sediment flux

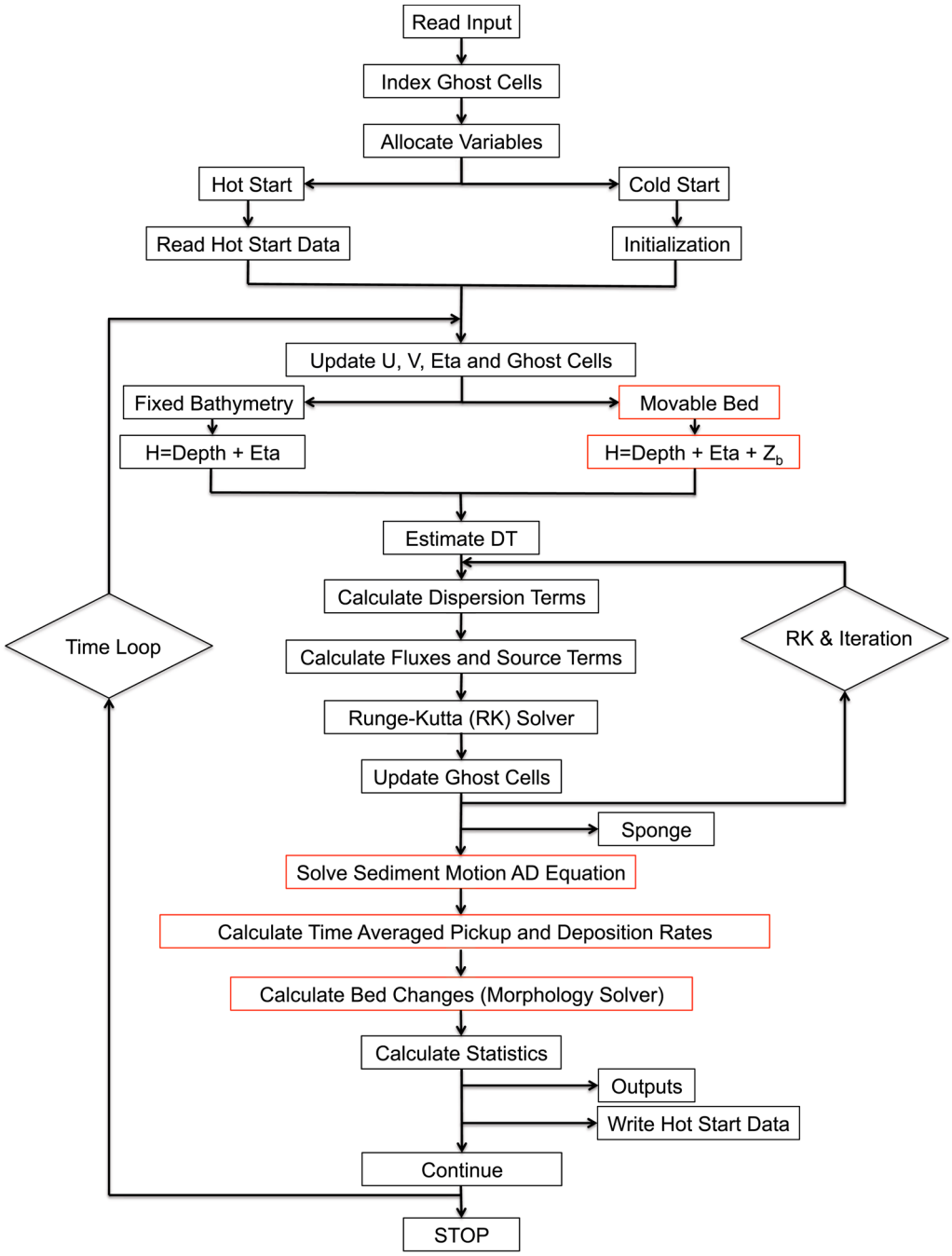

Figure 17
Flow chart for FUNWAVE-TVD. Red boxes indicate where modifications are made to implement sediment module

$$\mathbf{F} = C\mathbf{M} - kH\nabla_h C \tag{33}$$

where $C = \bar{c}/\rho_s$. The diffusion coefficient (k) used in (33) is calculated at cell faces using (14). The source term S on the right-hand side of (31) is the difference between the pickup rate P and the deposition rate D at the center of each cell,

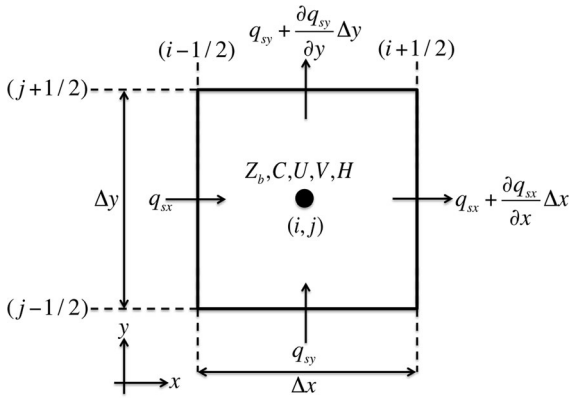

Figure 18
The regular grid used in FUNWAVE-TVD with velocities, sediment concentration, and depth values at the cell center and the fluxes on the cell faces

$$S = P - D \tag{34}$$

The pickup rate P is calculated at the cell centers, using Van Rijn (1986)'s formula (21), and the deposition rate (D) is also calculated at the cell centers using (30).

Appendix A5: Morphology Module

The sediment continuity equation (7) is solved to calculate depth changes z_b. Time-averaged sediment transport rates $(\bar{P}, \bar{D})$ are computed from instantaneous transport rate values (P, D) calculated in the sediment transport module, and are used in the sediment continuity equation to calculate bed changes. Following this approach, the discretized form of the sediment continuity equation can be written as,

$$\left(\frac{\Delta h}{\Delta t_{morph}}\right)^{k}_{i,j} = \frac{1}{1-n}\left(\bar{P}^{k}_{i,j} - \bar{D}^{k}_{i,j}\right) \tag{35}$$

The averaged transport rates were calculated using the following approach,

$$\bar{P}^{k}_{i,j} = \frac{1}{N}\sum_{l=1}^{N} P^{l}_{i,j} \tag{36}$$

$$\bar{D}^{k}_{i,j} = \frac{1}{N}\sum_{l=1}^{N} D^{l}_{i,j} \tag{37}$$

where,

$$N = \frac{\Delta t_{morph}}{\Delta t} \tag{38}$$

where N is defined as an input in the model with suggested values in the range of 5–20. The updated bed elevation is calculated using a third order Strong Stability-Preserving (SSP) Runge-Kutta scheme.

The still water depth h is updated for the hydrodynamic part of the model before the next time step calculations. Considering that the bed evolution scheme uses time averaged deposition and pickup rates $(\bar{D}, \bar{P})$ over a larger time step, the bed changes occur with a short lag compared to sediment suspension process. This lag difference introduces mass conservation problems close to the shoreline, because the morphology module does not march forward with the hydrodynamics and sediment transport module. Because $N = dt_{morph}/dt$ is a number between 5 and 20, a grid point close to the shoreline could fall into either a dry or wet region for different portions of a morphology time step.

In practice, the resulting errors are found to be negligible, as shown in Tehranirad et al. (2016).

Appendix A6: Non-erodible Beds

The sand layer thickness at each grid point $h_s - h$ (shown in Fig. 17) can be defined as an input for the model to indicate the locations of exposed hard bottom at the start of the simulation. The areas where $h = h_s$ are considered to be non-erodible. This condition can occur after the sediment layer is completely eroded or as an initial condition for regions with no sand, such as street pavements. When the hard bottom is exposed, the upward sediment flux (Pickup rate) is set to be zero in both Upwind and MUSCL-TVD schemes for the sediment transport module, as well as time-averaged pickup rate $\bar{P}$ used in sediment continuity equation. This condition is implemented in the model using the following expression,

$$P^{k}_{i,j} = \bar{P}^{k}_{i,j} = 0.0; \qquad h^{k}_{i,j} = h_{s_{i,j}}, \tag{39}$$

which ensures that the depth change is equal to or smaller than the sand layer thickness $h_s - h$.

References

Abdolali, A., & Kirby, J. T. (2017). Role of compressibility on tsunami propagation. *Journal of Geophysical Research: Oceans*, *122*(12), 9780–9794.

Abdolali, A., Kadri, U., & Kirby, J. T. (2019). Effect of water compressibility, sea-floor elasticity, and field gravitational potential on tsunami phase speed. *Scientific Reports*, *9*(1), 1–8.

Admire, A. R., Dengler, L. A., Crawford, G. B., Uslu, B., Borrero, J. C., Greer, S. D., et al. (2014). Observed and modeled currents from the tohoku-oki, japan and other recent tsunamis in northern california. *Pure and Applied Geophysics*, *171*(12), 3385–3403.

Allgeyer, S., & Cummins, P. R. (2014). Numerical tsunami simulation including elastic loading and seawater density stratification. *Geophysical Research Letters*, *41*, 2368–2375.

Amante, C., & Eakins, B. (2009). Etopo1 1 arc-minute global relief model: Procedures, data sources and analysis. In Tech. Rep. NOAA Technical Memorandum NESDIS NGDC-24, National Geophysical Data Center, NOAA.

Apotsos, A., Buckley, M., Geklfenbaum, G., Jaffe, B., & Vatvani, D. (2011). Nearshore tsunami inundation model validation: Toward sediment teansport applications. *Pure and Applied Geophysics*, *168*, 2097–2119.

Buttolph, A., Reed, C., Kraus, N., Ono, N., Larson, M., Camenen, B., Hanson, H., Wamsley, T., & Zundel, A. (2006). Two-dimensional depth-averaged circulation model CMS-M2D: Version 3.0, report 2, sediment transport and morphology change. In Tech. Rep. ERDC/CHL-TR-06-9., Engineer Research and Development Center Vicksburg MS Coastal and Hydraulics Lab.

Cao, Z. (1999). Equilibrium near-bed concentration of suspended sediment. *Journal of Hydraulic Engineering*, *125*, 1270–1278.

Chen, Q. (2006). Fully nonlinear Boussinesq-type equations for waves and currents over porous beds. *Journal of Engineering Mechanics*, *132*, 220–230.

Choowong, M., Murakoshi, N., Hisada, K., Charusiri, P., Charoentitirat, T., Chutakositkanon, V., et al. (2008). 2004 Indian Ocean Tsunami inflow and outflow at Phuket, Thailand. *Marine Geology*, *248*, 179–192.

Elder, J. W. (1959). The dispersion of marked fluid in turbulent shear flow. *Journal of Fluid Mechanics*, *5*, 544–560.

Fenster, M. S., Dolan, R., & Smith, J. J. (2016). Grain-size distributions and coastal morphodynamics along the southern Maryland and Virginia barrier islands. *Sedimentology*, *63*(4), 809–823.

Foster, D. L., Bowen, A. J., Holman, R. A., & Natoo, P. (2006). Field evidence of pressure gradient induced incipient motion. *Journal of Geophysical Research*, *111*, C05004. https://doi.org/10.1029/2004JC002863.

Fritz, H. M. (2011). Insights on the 2009 South Pacific tsunami in Samoa and Tonga from field surveys and numerical simulations. *Earth-Science Reviews*, *107*, 66–75.

Gelfenbaum, G., & Jaffe, B. (2003). Erosion and sedimentation from the 17 July, 1998 Papua New Guinea tsunami. *Pure and Applied Geophysics*, *160*, 1969–1999. https://doi.org/10.1007/s00024-003-2416-y.

Goto, K., Takahashi, J., Oie, T., & Imamura, F. (2011). Remarkable bathymetric change in the nearshore zone by the 2004 Indian Ocean tsunami: Kirinda Harbor, Sri Lanka. *Geomorphology*, *127*, 107–116. https://doi.org/10.1016/j.geomorph.2010.12.011.

Goto, K., Chagué-Goff, C., Goff, J., & Jaffe, B. (2012a). The future of tsunami research following the 2011 Tohoku-oki event. *Sedimentary Geology*, *282*, 1–13.

Goto, K., Sugawara, D., Abe, T., Haraguchi, T., & Fujino, S. (2012b). Liquefaction as an important source of the AD 2011 Tohoku-oki tsunami deposits at Sendai Plain, Japan. *Geology*, *40*(10), 887–890. https://doi.org/10.1130/G33123.1.

Grilli, S. T., Dubosq, S., Pophet, N., Perignon, Y., Kirby, J. T., & Shi, F. (2010). Numerical simulation and first-order hazard analysis of large co-seismic tsunamis generated in the Puerto Rico trench: Near-field impact on the North shore of Puerto Rico and far-field impact on the US East Coast. *Natural Hazards and Earth System Sciences*, *10*, 2109–2125.

Grilli, S. T., Harris, J. C., Tajalli Bakhsh, T., Masterlark, T. L., Kyriakopoulos, C., Kirby, J. T., et al. (2013). Numerical simulation of the 2011 Tohoku tsunami based on a new transient FEM co-seismic source: Comparison to far- and near-field observations. *Pure and Applied Geophysics*, *170*, 1333–1359. https://doi.org/10.1007/s00024-012-0528-y.

Grilli, S. T., O'Reilly, C., Harris, J. C., Tajalli Bakhsh, T., Tehranirad, B., Banihashemi, S., et al. (2015). Modeling of SMF tsunami hazard along the upper US East Coast: detailed impact around Ocean City, MD. *Natural Hazards*, *76*, 705–746. https://doi.org/10.1007/s11069-014-1522-8.

Grothe, P. R., Taylor, L. A., Eakins, B. W. , Carignan, K. S., Caldwell, R. J., Lim, E., & Friday, D. Z. (2011). Digital elevation models of Crescent City, California: Procedures, data and analysis. In NOAA Technical Memorandum NESDIS NGDC-51, Dept. of Commerce, Boulder, CO.

Grothe, P. R., Taylor, L. A., Eakins, B. W., Warnken, R. R., Carignan, K. S., Lim, E., Caldwell, R. J., & Friday, D. Z. (2010). Digital elevation model of Ocean City, Maryland: Procedures, data and analysis. In NOAA Technical Memorandum NESDIS NGDC-37, Dept. of Commerce, Boulder, CO.

Gusman, A. R., Goto, T., Satake, K., Takahashi, T., & Ishibe, T. (2018). Sediment transport modeling of multiple grain sizes for the 2011 tohoku tsunami on a steep coastal valley of numanohama, northeast japan. *Marine Geology*, *405*, 77–91.

Haraguchi, T., Goto, K., Sato, M., Yoshinaga, Y., Yamaguchi, N., & Takahashi, T. (2012). Large bedform generated by the 2011 Tohoku-oki tsunami at Kesennuma Bay, Japan. *Marine Geology*, *335*, 200–205. https://doi.org/10.1016/j.margeo.2012.11.005.

Hori, K., Kuzumoto, R., Hirouchi, D., Umitsu, M., Janjirawuttikul, N., & Patanakanog, B. (2007). Horizontal and vertical variation of 2004 Indian tsunami deposits: an example of two transects along the western coast of Thailand. *Marine Geology*, *239*, 163–172.

Horrillo, J., Knight, W., & Kowalik, Z. (2008). Kuril Islands tsunami of Novemebr 2006: 2. Impact at Crescent City by local enhancement. *Journal of Geophysical Research*, *113*, C01021. https://doi.org/10.1029/2007JC004404.

Jaffe, B., & Gelfenbaum, G. (2007). A simple model for calculating tsunami flow speed from tsunami deposits. *Sedimentary Geology*, *200*, 347–361. https://doi.org/10.1016/j.sedgeo.2007.01.013.

Kim, D. H. (2015). H2d morphodynamic model considering wave, current and sediment interaction. *Coastal Engineering*, *95*, 20–34.

Kim, D. H., Lynett, P. J., & Socolofsky, S. A. (2009). A depth-integrated model for weakly dispersive, turbulent, and rotational fluid flows. *Ocean Modelling*, *27*(3–4), 198–214. https://doi.org/10.1016/j.ocemod.2009.01.005.

Kim, D. H., Sanchez-Arcilla, A., & Caceres, I. (2017). Depth-integrated modelling on onshore and offshore sandbar migration: Revision of fall velocity. *Ocean Modelling*, *110*, 21–31. https://doi.org/10.1016/j.ocemod.2016.12.011.

Kirby, J. T., Shi, F., Tehranirad, B., Harris, J. C., & Grilli, S. T. (2013). Dispersive tsunami waves in the ocean: Model equations and sensitivity to dispersion and Coriolis effects. *Ocean Modelling*, *62*, 39–55.

Klonaris, G. T., Memos, C. D., Dronen, N. K., & Deigaard, R. (2017). Boussinesq-type modelling of sediment transport and coastal morphology. *Coastal Engineering Journal*, *59*(1), 1750007. https://doi.org/10.1142/S0578563417500073.

Kobayashi, N., & Lawrence, A. R. (2004). Cross-shore sediment transport under breaking solitary waves. *Journal of Geophysical Research*, *109*, C03047. https://doi.org/10.1029/2003JC002084.

Kowalik, Z., Horrillo, J., Knight, W., & Logan, T. (2008). Kuril Islands tsunami of November 2006: 1. Impact at Crescent City by distant scattering. *Journal of Geophysical Research*, *113*, C01020. https://doi.org/10.1029/2007JC004402.

Lander, J. F., Lockridge, P. A., & Kozuch, M. J. (1993). Tsunamis affecting the West Coast of the United States. In US Dept of Commerce, National Oceanic and , vol. 29, pp. 1806–1992.

Larson, M., & Kraus, N. C. (1989). SBEACH: numerical model for simulating storm-induced beach change. In Report 1. Empirical foundation and model development. No CERC-TR-89-9 Coastal Engineering Research Center Vicksburg Ms.

Lee, J., Huang, Z., Kou, Z., & Xing, X. (2012). The effect of tide level on the tsunami response of coastal harbors. *Coastal Engineering Proceedings*, *1*(33), 11.

Li, L., & Huang, Z. (2013). Modeling the change of beach profile under tsunami waves: A comparison of selected sediment transport models. *Journal of Earthquake and Tsunami*, *7*, 1350001.

Long, W., Kirby, J. T., & Hsu, T. J. (2006). Cross shore sandbar migration predicted by a time domain Boussinesq model incorporating undertow. In Proceedings of the 30th Intenational Conference on Coastal Engineering, San Diego, CA, pp. 2655–2667.

Naruse, H., & Abe, T. (2017). Inverse tsunami flow modeling including non-equilibrium sediment transport, with application to deposits from the 2011 Tohoku-Oki tsunami. *Journal of Geophysical Research: Earth Surface*, *122*(11), 2159–2182. https://doi.org/10.1002/2017JF004226.

Nwogu, O. (1993). An alternative form of the Boussinesq equations for nearshore wave propagation. *Journal of Waterway, Port, Coastal, and Ocean Engineering*, *119*, 618–638.

Pintado-Patiño, J. C. (2017). Procesos dinámicos en la zona de swash: un estudio integral. In PhD thesis, Universidad Nacional Autónoma do México.

Rahman, S., Mano, A., & Udo, K. (2012). Coupling of Boussinesq and sediment transport model in a wave flume. *Journal of the Japanese Society of Civil Engineers*, *68*, 259–264.

Ramalho, I., Omira, R., El Moussaoui, S., Baptista, M., & Zaghloul, M. (2018). Tsunami-induced morphological change-a model-based impact assessment of the 1755 tsunami in ne atlantic from the morocco coast. *Geomorphology*, *319*, 78–91.

Rasyif, T. M., Kato, S., Okabe, T., et al. (2019). Numerical simulation of morphological changes due to the 2004 tsunami wave around banda aceh, indonesia. *Geosciences*, *9*(3), 125.

Rubey, W. W. (1933). Settling velocity of gravel, sand and silt particles. *American Journal of Science*, *148*, 325–338.

Sanchez, A., Wu, W., & Beck, T. M. (2016). A depth-averaged 2-d model of flow and sediment transport in coastal waters. *Ocean Dynamics*, *66*, 1475–1495. https://doi.org/10.1007/s10236-016-0994-3.

Shi, F., Kirby, J. T., Harris, J. C., Geiman, J. D., & Grilli, S. T. (2012). A high-order adaptive time-stepping TVD solver for Boussinesq modeling of breaking waves and coastal inundation. *Ocean Modelling*, *43–44*, 36–51. https://doi.org/10.1016/J.OCEMOD.2011.12.004.

Sleath, J. F. A. (1999). Conditions for plug flow formation in oscillatory flow. *Continental Shelf Research*, *19*, 1643–1664.

Son, S., & Jung, H. T. (2015). 2HD analysis of morphologic responses to the tsunami impacts using process-based model. *Procedia Engineering*, *116*, 979–985. https://doi.org/10.1016/j.proeng.2015.08.389.

Sugawara, D., Goto, K., & Jaffe, B. E. (2014a). Numerical models of tsunami sediment transport—current understanding and future directions. *Marine Geology*, *352*, 295–320. https://doi.org/10.1016/j.margeo.2014.02.007.

Sugawara, D., Takahashi, T., & Imamura, F. (2014b). Sediment transport due to the 2011 Tohoku-oki tsunami at Sendai: Results from numerical modeling. *Marine Geology*, *358*, 18–37. https://doi.org/10.1016/j.margeo.2014.05.005.

Sumer, B. M., Kozakiewicz, A., Fredsøe, J., & Deigaard, R. (1996). Velocity and concentration profiles in sheet-flow layer of movable bed. *Journal of Hydraulic Engineering*, *122*(10), 549–558.

Szczuciński, W., Kokociński, M., Rzeszewski, M., Chagué-Goff, C., Cachão, M., Goto, K., et al. (2012). Sediment sources and sedimentation processes of 2011 Tohoku-oki tsunami deposits on the Sendai Plain, Japan, insights from diatoms, nannoliths and grain size distribution. *Sedimentary Geology*, *282*, 40–56. https://doi.org/10.1016/j.sedgeo.2012.07.019.

Takashimizu, Y., Urabe, A., Suzuki, K., & Sato, Y. (2012). Deposition by the 2011 Tohoku-oki tsunami on coastal lowland controlled by beach ridges near Sendai, Japan. *Sedimentary Geology*, *282*, 124–141. https://doi.org/10.1016/j.sedgeo.2012.07.004.

Tanaka, N., & Sato, M. (2015). Scoured depth and length of pools and ditches generated by overtopping flow from embankments during the 2011 Great East Japan tsunami. *Ocean Engineering*, *109*, 72–82. https://doi.org/10.1016/j.oceaneng.08.053.

Tanaka, H., Tinh, N. X., Umeda, M., Hirao, R., Pradjoko, E., Mano, A., et al. (2012). Coastal and estuarine morphology changes induced by the 2011 Great East Japan Earthquake Tsunami. *Coastal Engineering Journal*, *54*(01), 1250010.

Tappin, D. R., Grilli, S. T., Harris, J. C., Geller, R. J., Masterlark, T., Kirby, J. T., et al. (2014). Did a submarine landslide contribute to the 2011 Tohoku tsunami? *Marine Geology*, *357*, 344–361. https://doi.org/10.1016/j.margeo.2014.09.043.

Tehranirad, B., Banihashemi, S., Kirby, T. J., Callahan, J., & Shi, F. (2014). Tsunami inundation mapping for Ocean City, MD NGDC DEM. In Research Report CACR-14-04, Center for

Applied Coastal Research, Department of Civil and Environmental Engineering, University of Delaware.

Tehranirad, B., Kirby, J. T., & Shi, F. (2016). Does morphology adjustment during tsunami inundation increase levels of hazard? Research Report CACR-16-02, Center for Applied Coastal Research, Department of Civil and Environmental Engineering, University of Delaware.

Tehranirad, B., Kirby, T. J., Callahan, J., & Shi, F. (2015b). Tsunami inundation mapping for Atlantic City, NJ NGDC DEM. In Research CACR-15-01, Center for Applied Coastal Research, Department of Civil and Environmental Engineering, University of Delaware.

Tehranirad, B., Kirby, J. T., Grilli, S. T., & Shi, F. (2017). Does a morphological adjustment during Tsunami inundation increase levels of hazards? In Coastal structures and solutions to coastal disasters 2015: Tsunamis, (pp. 145–153). Reston, VA: American Society of Civil Engineers.

Tehranirad, B., Harris, J. C., Grilli, A. R., Grilli, S. T., Abadie, S., Kirby, J. T., et al. (2015a). Far-field tsunami impact in the North Atlantic basin from large scale flank collapses of the Cumbre Vieja volcano, La Palma. *Pure and Applied Geophysics*, *172*, 3589–3616. https://doi.org/10.1007/s00024-015-1135-5.

Teran Cobo, P., Kirby, J. T., Haller, M. C., Özkan Haller, H. T., Magallen, J., & Guannel, G. (2006). Model simulations of bar evolution in a large scale laboratory beach. In Proceedings of the 30th Intenational Conference on Coastal Engineering (pp. 2566–2578). San Diego: World Scientific.

Udo, K., Sugawara, D., Tanaka, H., Imai, K., & Mano, A. (2012). Impact of the 2011 Tohoku earthquake and tsunami on beach morphology along the northern Sendai coast. *Coastal Engineering Journal*, *54*, 1250009. https://doi.org/10.1142/S057856341250009X.

Udo, K., Takeda, Y., & Tanaka, H. (2016). Coastal morphology change before and after 2011 Off the Pacific Coast of Tohoku earthquake tsunami at Rikuzen-Takata coast. *Coastal Engineering Journal*, *58*(4), 1640016. https://doi.org/10.1142/S0578563416400167.

Van Rijn, L.C, & Tan G.L. (1985). *Two-dimensional vertical mathematical model for suspended sediment transport by currents and waves*. Rijkswaterstaat Communciations 41, Hydraulics Laboratory. http://resolver.tudelft.nl/uuid:bea0d9e0-2559-403d-b03d-e4045dbec8ca.

Van Rijn, L. C. (1984). Sediment transport, part II: Suspended load transport. *Journal of hydraulic engineering*, *110*(11), 1613–1641.

Van Rijn, L. C. (1986). Applications of sediment pick-up function. *Journal of Hydraulic Engineering*, *112*(9), 867–874.

Van Rijn, L. C. (2007a). Unified view of sediment transport by currents and waves. I: Initiation of motion, bed roughness, and bed-load transport. *Journal of Hydraulic Engineering*, *133*(6), 649–667.

Van Rijn, L. C. (2007b). Unified view of sediment transport by currents and waves. II: Suspended transport. *Journal of Hydraulic Engineering*, *133*(6), 668–689.

Wang, D. (2015). An ocean depth-correction method for reducing model errors in tsunami travel time: Application to the 2010 Chile and 2011 Tohoku tsunamis. *Science of Tsunami Hazards*, *34*(1), 1–22.

Wilson, R., Davenport, C., & Jaffe, B. (2012). Sediment scour and deposition within harbors in California (USA), caused by the March 11, 2011 Tohoku-oki tsunami. *Sedimentary Geology*, *282*, 228–240. https://doi.org/10.1016/j.sedgeo.2012.06.001.

Wilson, R. I., Admire, A. R., Borrero, J. C., Dengler, L. A., Legg, M. R., Lynett, P., et al. (2013). Observations and impacts from the 2010 Chile and 2011 Japanese tsunamis in California (USA). *Pure and Applied Geophysics*, *170*, 1127–1147. https://doi.org/10.1007/s00024-012-0527-z.

Yamashita, K., Sugawara, D., Takahashi, T., Imamura, F., Saito, Y., Imato, Y., et al. (2016). Numerical simulations of large-scale sediment transport caused by the 2011 Tohoku Earthquake Tsunami in Hirota Bay, Southern Sanriku Coast. *Coastal Engineering Journal*, *58*(04), 1640015.

Yeh, H., Robertson, I., & Preuss, J. (2005). Development of design guidelines for structures that serve as tsunami vertical evacuation sites. In Tech. rep., Washington State Department of Natural Resources, Division of Geology and Earth Resources.

(Received April 13, 2020, revised August 27, 2020, accepted October 23, 2020, Published online November 11, 2020)